Publ. Astron. Soc. Japan (2020) 72 (4), 55 (1–22)
doi: 10.1093/pasj/psaa048
Advance Access Publication Date: 2020 June 11

Star formation rates in the L 1482 filament of the California molecular cloud

Toshihiro OMODAKA,[1,*] Takumi NAGAYAMA,[2] Kazuhito DOBASHI,[3] James O. CHIBUEZE,[4,5] Akifumi YAMABI,[3] Yoshito SHIMAJIRI,[6] Shinnosuke INOUE,[1] Shota HAMADA,[1] Kazuyoshi SUNADA,[2] and Yuji UENO[2]

[1]Department of Physics and Astronomy, Graduate School of Science and Engineering, Kagoshima University, 1-21-35 Korimoto, Kagoshima, Kagoshima 890-0065, Japan
[2]Mizusawa VLBI Observatory, National Astronomical Observatory of Japan, 2-21-1 Osawa, Mitaka, Tokyo 181-8588, Japan
[3]Department of Astronomy and Earth Sciences, Tokyo Gakugei University, Koganei, Tokyo 184-8501, Japan
[4]Centre for Space Research, Physics Department, North-West University, Potchefstroom 2520, South Africa
[5]Department of Physics and Astronomy, Faculty of Physical Sciences, University of Nigeria, Carver Building, 1 University Road, Nsukka, Nigeria
[6]National Astronomical Observatory of Japan, 2-21-1 Osawa, Mitaka, Tokyo 181-8588, Japan

*E-mail: omodaka.toshihiro@gmail.com

Received 2020 February 21; Accepted 2020 April 20

Abstract

We measured the trigonometric parallax of the H_2O maser source associated with the L 1482 molecular filament hosting the most massive young star, LkHα 101, in the California molecular cloud. The measured parallax is 1.879 ± 0.096 mas, corresponding to the distance of 532 ± 28 pc. This parallax is consistent with that of the nearby star cluster LkHα 101, which was recently measured with Gaia DR2. We found that the L 1482 molecular filament and the LkHα 101 cluster are located at the same distance within 3 ± 30 pc. We observed the southern parts of L 1482 molecular clouds including the H_2O maser source, which is adjacent to LkHα 101, using the Nobeyama 45 m telescope in the $J = 1$–0 transitions of both ^{12}CO and ^{13}CO. The peak intensity of the ^{12}CO line revealed the high excitation temperature region (60–70 K) due to heating by UV radiation from LkHα 101. We derived the column density of these molecular clouds assuming local thermodynamic equilibrium (LTE) from the ^{13}CO emission. Using Dendrogam, we searched for small-scale, dense structures (cores) and identified 337 cores in the ^{13}CO data. Gravitationally bound cores with a virial mass to LTE mass ratio $\leq$1.5 and young stars are concentrated in the high excitation temperature region. The column density in the warm region is five to six times larger than that of the surrounding colder molecular region. This suggests that the warm region has been compressed by a high-pressure wave and successive radiation-driven star formation is in progress in this warm region. In the cold molecular cloud to the north of the warm region, the cores are likely gravitationally unbound, which may be the reason why star formation is not active there.

Key words: astrometry — ISM: clouds — masers — stars: formation — stars: individual (LkHα 101)

1 Introduction

The formation process of massive stars in giant molecular clouds is important but poorly understood phenomenon. As described by Lada, Lombardi, and Alves (2009), the California Molecular Cloud (CMC) rivals the well-known massive star-forming region, the Orion Molecular Cloud (OMC) as the most massive giant molecular cloud with similar mass, size, filamentary structure, and morphology. However, despite its large mass, the CMC is characterized by a star formation rate (SFR) that is an order of magnitude lower than that of the OMC. The most massive star that is forming in the CMC is an early B star, LkHα 101, embedded in a cluster of lower-mass young stars (Andrews & Wolk 2008). The study of star formation in the CMC is very important due to its marked contrast to that of the OMC. The CMC is characterized by filamentary structures, with L 1482 being one of the prominent filaments in the region. LkHα 101 is a member of the embedded star cluster of young low-mass stars in the south-eastern part of L 1482 and is likely an early B star ($M \sim 15\,M_{\odot}$, Herbig et al. 2004). The most prominent feature is a dark lane of L 1482 which runs across the southeastern corner of the LkHα 101 cluster (Andrews & Wolk 2008). Since the LkHα 101 cluster is at the junction of two molecular filaments, L 1482 filament 1 and filament 2 on the plane of the sky, Li et al. (2014) suggested that the origin of the LkHα 101 cluster might be merging molecular filaments fed by converging inflows. However, Redman et al. (1986) argued that the dark lane is in the foreground and probably not associated with the LkHα 101 cluster. That argument is further supported by the interstellar H^+ chemistry constraints in the vicinity of an intense radiation source (Brittain et al. 2004). Accurate distances of both the LkHα 101 cluster and L 1482 filaments are required to understand star formation in the region.

Recently, the parallax of VLA J043001.15+337724.6, which is a member of the LkHα 101 cluster, was measured to be 1.87 ± 0.10 mas (corresponding to the distance of 532 ± 28 pc) with Very Long Baseline Array (VLBA) radio continuum observations (Dzib et al. 2018). The astrometric result of Gaia DR2 (Gaia Collaboration 2018) also contains the measured parallax of the LkHα 101 cluster. H_2O masers were detected in L 1482 filament 2 (Sunada et al. 2007), thus we made its parallax measurement with the VLBI astrometric observations to compare the distances of the LkHα 101 star cluster and the L 1482 molecular filament directly. If LkHα 101 is adjacent to L 1482, LkHα 101 (B star) and the intense radiation pressure from it will have a significant effect on the surrounding gas and form the H II region. The cloud surface adjacent to the H II region is photo-dissociated by the ultraviolet (UV) and far-UV (FUV). Recently, Goicoechea et al. (2016) observed the Orion Bright Bar photo-dissociated region (PDR) using the ALMA telescope; the warm cloud edge, exposed to energetic radiation from the Trapezium stars, revealed a fragmented ridge of high-density substructures and photo-ablative gas flows. They suggest that the cloud edge has been compressed by a high-pressure wave moving into the molecular cloud. The warm PDR adjacent to LkHα 101 is a similar physical region to the Orion Bar PDR. In this warm region, successive star formation may be triggered due to radiation-driven star formation.

In this paper, we study the star formation in the warm region facing to the LkHα 101 cluster. We observed molecular regions adjacent to LkHα 101 using the Nobeyama 45 m telescope in the J = 1–0 transitions of ^{12}CO and ^{13}CO. By using the ^{13}CO data, we derived the column density of the molecular clouds assuming local thermodynamic equilibrium (LTE). We executed Dendrogam analysis to identify gravitationally unstable dense cores. We explored the evolution of star formation in the California Molecular Cloud, We explored the evolution of star formation in the California Molecular Cloud, which Lada et al. (2009) referred to as a sleeping giant molecular cloud.

2 Observations and data reduction

2.1 VERA telescope

The VLBI observations of the 22.235080 GHz H_2O maser in L 1482 were carried out on 2010/333, 2011/016, 2011/113, 2011/228, 2011/297, and 2011/353 (year/day of the year) with VERA. The observing time was approximately eight hours at each epoch. VERA is a Japanese VLBI array, which consists of four 20 m diameter antennas in Mizusawa, Iriki, Ogasawara, and Ishigaki-jima, with 2300 km maximum and 1200 km minimum baseline lengths (Omodaka 2009) VERA has a dual-beam system, which allows simultaneously observing of adjacent sources (target maser and position reference sources within $2\overset{\circ}{.}2$ separation) for the purpose of correcting for the tropospheric fluctuations (Kawaguchi et al. 2000). The target source, L 1482, and the position reference source, J0429+3319, which is listed in the second realization of the International Celestial Reference Frame (ICRF2), were simultaneously observed using the dual-beam system of VERA. The separation angle between the target and the position reference source is $1\overset{\circ}{.}84$. The data correlation was carried out with the FX-type hardware correlator at the Mitaka campus of the National Astronomical Observatory of Japan (NAOJ) (Chikada et al. 1991). The phase tracking centers of L 1482 and J0429+3319 are $(\alpha, \delta)_{\rm J2000.0} = (04^{\rm h}30^{\rm m}27\overset{\rm s}{.}4008,\ +35^{\circ}09'17\overset{\prime\prime}{.}649)$ and

($04^h29^m52\overset{s}{.}721121$, $+33°19'01\overset{''}{.}85849$), respectively. The accumulation time of the correlation process was set to 1 s. The frequency and velocity spacing of L 1482 are 15.625 kHz and 0.21 km s^{-1}, respectively. The total bandwidth and the frequency spacing of J0429+3319 are 240 MHz and 0.25 MHz, respectively. Data reduction was done using VERA Data Analyzer (VEDA), which is a software package developed by the Mizusawa VLBI Observatory of NAOJ. The fringe search of J0429+3319 was done with an integration time of 128 s and a time interval of 32 s. The fringe and the self-calibration solutions of J0429+3319 were applied accordingly to L 1482. The peak intensity in the self-calibration map of J0429+3319 is approximately 0.07 Jy beam^{-1}. The instrumental delay and phase between the dual-beam is calibrated by the horn-on-dish method using the artificial noise source and the phase correction detector (Honma et al. 2008b). The tropospheric delay is calibrated using the tropospheric zenith delay measured by GPS (Honma et al. 2008a) and the tropospheric mapping function (Niell 1996). The ionospheric delay is calibrated using the Global Ionosphere Map (GIM) produced by the University of Bern.

2.2 CO observations with the Nobeyama 45 m radio telescope

Using the Nobeyama 45 m radio telescope, the ^{12}CO (J = 1–0) observations towards the $13' \times 12'$ region around L 1482 was carried out between 2013 March and May, while the ^{13}CO (J = 1–0) observations covering the $40' \times 40'$ region in the southern part of L 1482 were done between 2013 December and 2014 January. We used the new two-beam, two-polarization, side-band separating receiver, TZ, for the ^{12}CO (J = 1–0) observations, and the 25-element focal plane receiver, BEARS, installed in the 45 m telescope for the ^{13}CO (J = 1–0) observations. At 110 GHz, the telescope has a beam size of 16$''$ (half power beam width, HPBW). The beam separation of BEARS is $41\overset{''}{.}1$ on the plane of the sky (Sunada et al. 2000). The typical noise temperature was ∼150 K for the TZ receiver and 300 K for BEARS. The on-the-fly (OTF) technique was adopted to map each observation box. The temperature scale was determined by the chopper-wheel method. The telescope pointing was checked every hour by observing SiO maser line from Orion KL. The parameters of the observations are summarized in table 1.

Table 1. Observation parameters with the Nobeyama 45 m telescope.

Molecular line	^{12}CO (J = 1–0)	^{13}CO (J = 1–0)
Rest frequency (GHz)	115.271202	110.201353
Beam size ($''$)	14	15
Receiver	TZ	BEARS
Bandwidth (MHz)	63	32
Frequency resolution (kHz)	15.26	35.75
Velocity resolution (km s^{-1})	0.05	0.1
Map gird size	$7\overset{''}{.}5$	$7\overset{''}{.}5$
Noise level (K)	2.53	1.17
Map coverage	$13' \times 12'$	$40' \times 40'$

3 Results

3.1 Annual parallax

A maser spot at V_{LSR} = 7.38 km s^{-1} was detected over all six VLBI observation epochs. The peak intensities from the first to the last epochs were 2.37, 1.34, 1.80, 2.73, 9.21, and 7.24 Jy beam^{-1}. Figure 1 (left-hand panel) shows the phase-referenced map of this spot. The detected position of this H_2O maser spot, $(\alpha, \delta)_{J2000.0}$ = ($04^h30^m27\overset{s}{.}4008$, $+35°09'17\overset{''}{.}649$), is consistent within $0\overset{''}{.}2$ with that of the class I young stellar object (YSO) J04302741+3509178 (Broekhoven-Fiene et al. 2015) in L 1482 filament 2 (Li et al. 2014), the bolometric luminosity of which is 9.26 $L_\odot$ (Harvey et al. 2013). The H_2O maser is most likely associated with this YSO. The positional variation of this maser spot during the six epochs is shown in figure 2. Least-square fits were made to these positions, with the parallax, as well as the proper motion. The parallax and the proper motion were obtained to be $\pi = 1.879 \pm 0.096$ mas ($D = 532 \pm 28$ pc) and ($\mu_\alpha \cos\delta, \mu_\delta$) = ($3.17 \pm 0.16$, -8.55 ± 0.16) mas yr^{-1}, respectively. Systematic errors in (RA, Dec) of (0.127, 0.138) mas were added in quadrature to the formal errors calculated by $\sigma_{\rm formal} = \theta_{\rm beam}/(2 \times SNR)$ to achieve the reduced $\chi^2 = 1$.

3.2 CO excitation temperature

In order to demonstrate the observed ^{12}CO (J = 1–0) spectra, we divided the $13' \times 12'$ observed region into 10 × 10 grids, and in each grid we averaged the data. Figure 3 shows the averaged spectra. The peak intensity is 45 K and the average over the cloud is 23 K, and we show the ^{12}CO intensity distribution around LkHα 101 in figure 4. We estimated the excitation temperature $T_{\rm ex}$ on the assumption that the rotational levels of gas are in the LTE and that the ^{12}CO (J = 1–0) emission line is optically thick. $T_{\rm ex}$ is then given by

$$T_{\rm ex} = \frac{5.53}{\ln\left[1 + 5.53/(T_{\rm peak} + 0.819)\right]}\ {\rm K}, \quad (1)$$

where $T_{\rm peak}$ is the peak intensity of the ^{12}CO line in Kelvin. The average $T_{\rm ex}$ in this region is higher than 30 K (Kong et al. 2015) obtained over the vast majority of the CMC.

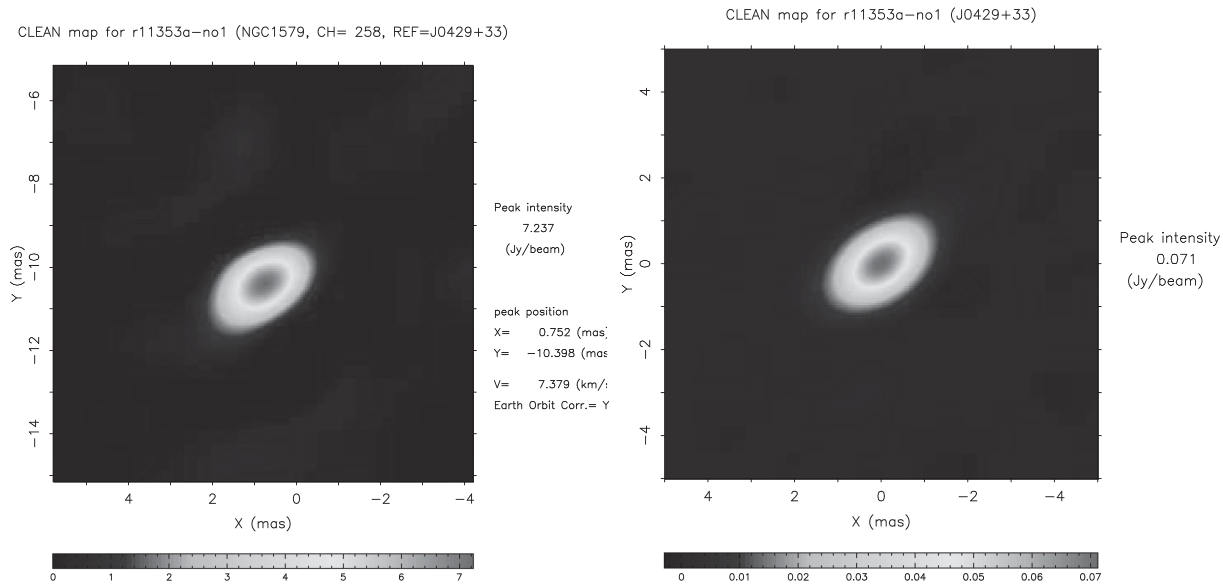

Fig. 1. Phase-referencing H_2O maser map of L 1482 (left) and self-calibrated image of the position reference source (J0429+3319) (right) from the 2011 day-353 epoch.

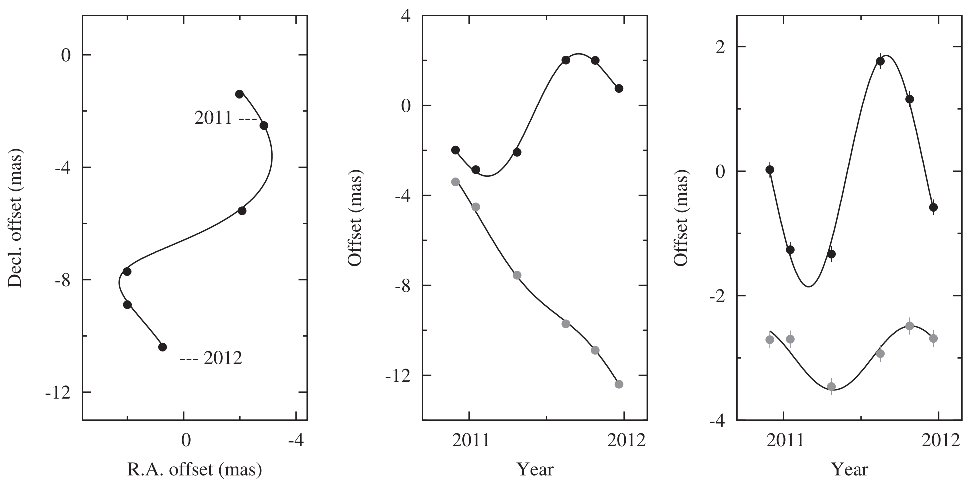

Fig. 2. Parallax and proper motion of the H_2O maser spot at $V_{LSR} = 7.38\,\mathrm{km\,s^{-1}}$ in L 1482. (Left) Positions on the sky. (Middle) RA (black circles) and Dec (gray circles) offset versus time. (Right) Same as the middle panel, but the proper motion of the target has been subtracted, leaving only the effect of the parallax.

The highest excitation temperatures obtained in the CMC are nearly ∼70 K.

Figure 5 shows the spatial distribution of the ^{13}CO (J = 1–0) spectra which we obtained by dividing the 40′ × 40′ observed region into 10 × 10 grids and by averaging the data in each grid. It is noted that the presence of an arc-shaped region (southward) with high excitation temperatures centering around LkHα 101, and we show the ^{13}CO intensity distribution in figure 6. A further interesting feature is the presence of a single self-absorption over the region facing the LkHα 101 cluster. Figure 7 shows the comparison of the ^{12}CO and ^{13}CO spectra. Clear dips in the ^{12}CO spectra can be recognized in the velocity range from $-1\,\mathrm{km\,s^{-1}}$ to $+1\,\mathrm{km\,s^{-1}}$. The velocities of these dips coincide with the peak velocities of the ^{13}CO spectra. This suggests that the ^{12}CO emission emitted from the warm region around LkHα 101 is absorbed by the colder gas in the foreground, because the line is optically thick.

As shown in the next subsection, we estimated the column densities of ^{13}CO, $N_{^{13}\mathrm{CO}}$, on the assumption of LTE. We used T_{ex} derived from the ^{12}CO data. However, the area mapped in ^{13}CO is much larger than that mapped in ^{12}CO. Li et al. (2014) carried out ^{12}CO(J = 3–2) observations toward L 1482, and covered an extent similar to our ^{13}CO map. They found that the strong ^{12}CO(J = 3–2)

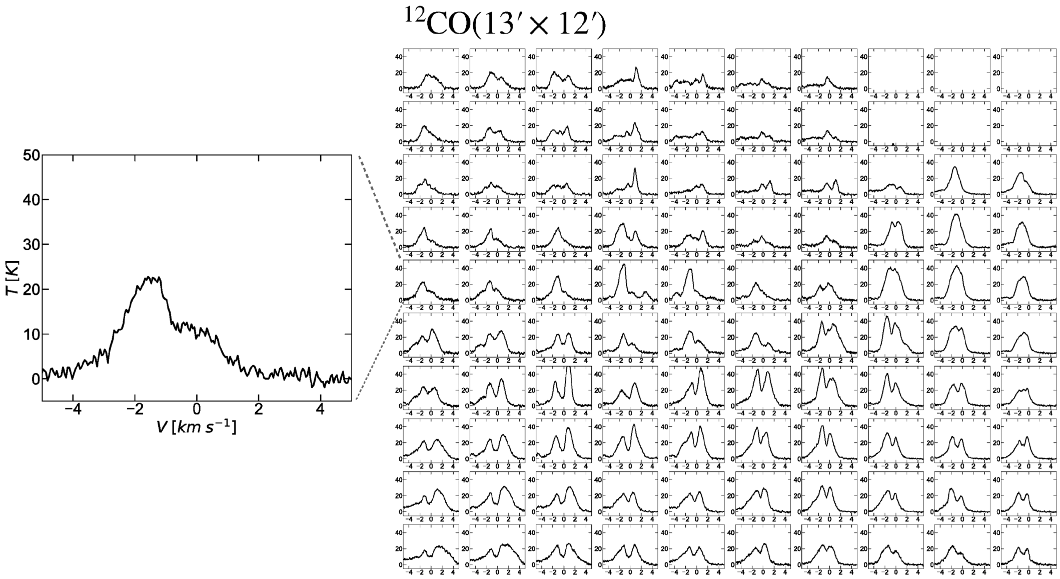

Fig. 3. Distribution of the observed ^{12}CO emission. The region mapped in ^{12}CO is 13′ × 12′ as shown in figure 4. We divided the region into 10 × 10 grids and calculated the average spectra, in each grid.

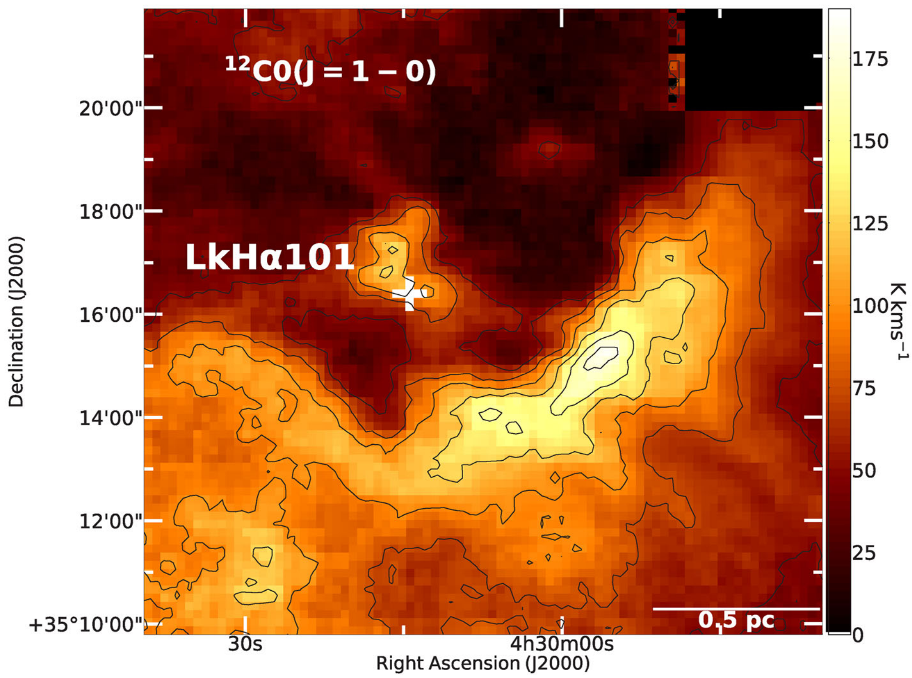

Fig. 4. Integrated intensity map of the ^{12}CO($J = 1$–0) emission line towards the L 1482 molecular cloud. The velocity used for the integration is from $-5\,\mathrm{km\,s^{-1}}$ to $+5\,\mathrm{km\,s^{-1}}$, and the size of map is 13′ × 12′. The contours start from $50\,\mathrm{K\,km\,s^{-1}}$ with an increment of $25\,\mathrm{K\,km\,s^{-1}}$.

emission is detected around the cloud (see, their figure 2) even in regions not covered by our ^{12}CO$J = 1$–0 observations. Since the energy necessary to excite the $J = 3$–2 transition is $h\nu/k \simeq 32\,\mathrm{K}$ in temperature, the regions emitting the molecular line should have an excitation temperature higher than this value. For regions not covered in our ^{12}CO observations, we therefore assumed a uniform T_{ex} of 35 K.

3.3 Dense cores in L 1482 filament: core identification and mass derivation

In order to study the star formation activity in the L 1482 filament, we identified cores using the fiducial core-finding algorithm Dendrogram, (Rosolowsky et al. 2008) implemented in the astrodendro python package. Dendrogram is a tree diagram that represents the hierarchy of structures

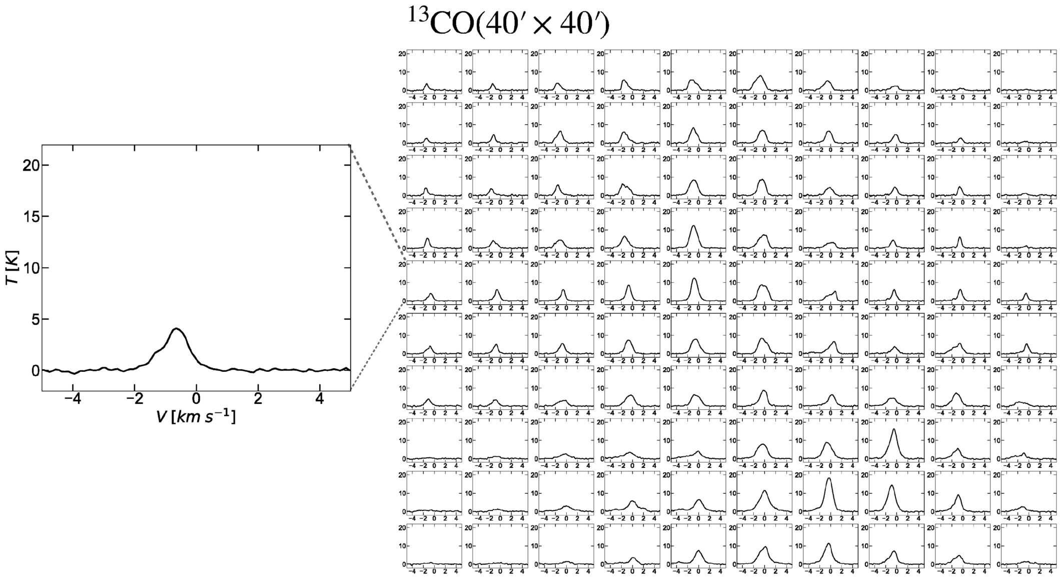

Fig. 5. Distribution of the observed ^{13}CO emission. The region mapped in ^{13}CO is 40′ × 40′ as shown in figure 6. We divided the region into 10 × 10 grids and calculated the average spectra, in each grid.

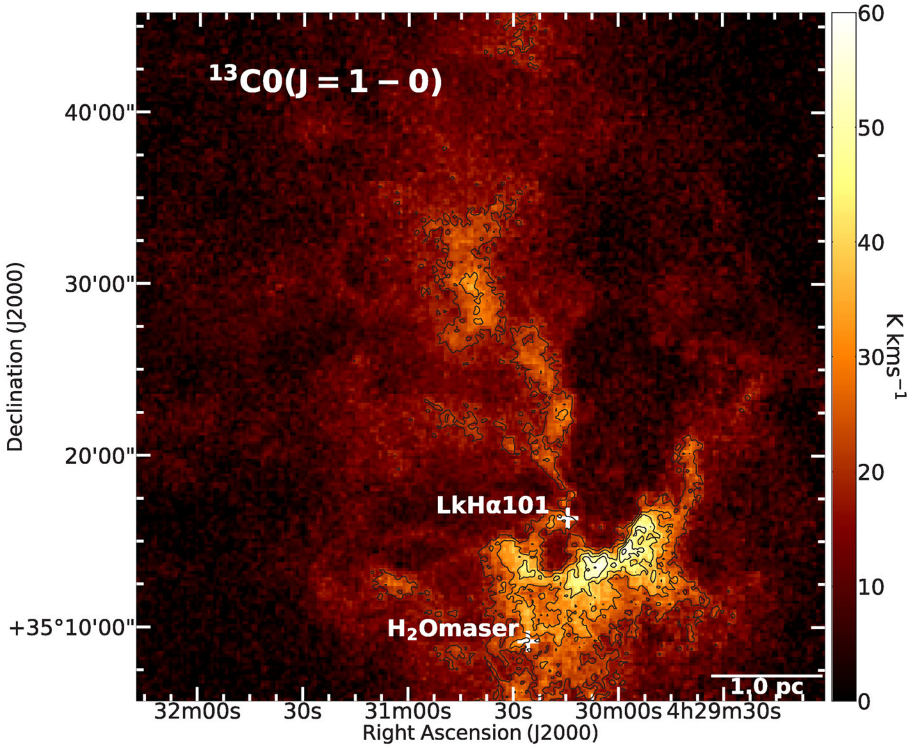

Fig. 6. Integrated intensity map of ^{13}CO (J = 1–0) emission line towards the L 1482 molecular cloud. The velocity range used for the integration is $-2.9\,\mathrm{km\,s^{-1}}$ to $+2.9\,\mathrm{km\,s^{-1}}$, and the size of map is 40′ × 40′. The contours start from $20\,\mathrm{K\,km\,s^{-1}}$ with an increment of $10\,\mathrm{K\,km\,s^{-1}}$.

within given data. It is composed of two types of structure, "branches" and "leaves." Branches are the structures that split into multiple sub-structures, and the leaves are the structures that have no sub-structure. In this study, we define the smallest structure "leaf" as a core, and focus on the detection of cores. We used the three-dimensional ^{13}CO data cube, which is an appropriate tracer to analyze internal structures through the entire molecular cloud, because the ^{13}CO emission line is moderately optically thin in the observed region, and is a good probe of the column density. To identify the cores, we applied Dendrogram to the ^{13}CO cube with parameters *min_value* of 5σ, *min_delta*

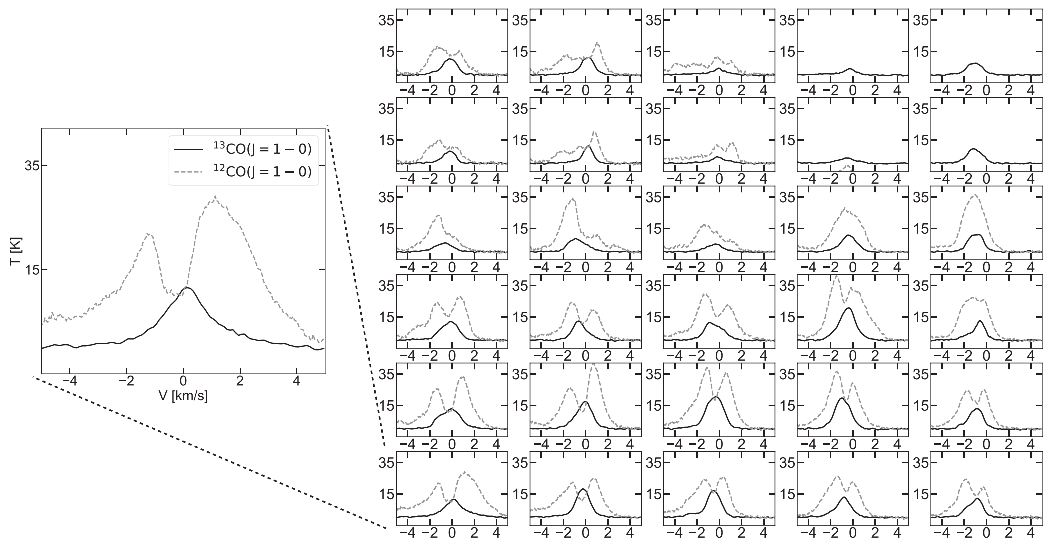

Fig. 7. Comparison of the ^{12}CO (dotted lines) and the ^{13}CO (solid lines) emission lines around LkHα 101. We divided the 13′ × 12′ area observed in ^{12}CO into 5 × 6 grids, and calculated the ^{12}CO and ^{13}CO spectra in each grid.

of 3σ, and *min_npix* of 5.2 pixels ($= A_{\theta_{\rm beam}}/A_{\rm pixel}$). We note that *min_npix* is the minimum number of pixels that the structures must contain. We used the signal-to-noise ratio map to avoid detection of fake sources due to the non-uniform noise distribution. The application of Dendrogram with these parameters to the ^{13}CO data cube resulted in the identification of 337 cores in a square region of $\sim 40' \times 40'$.

We derived the physical parameters of the cores assuming the LTE using the standard procedures (e.g., Wilson et al. 2009). Using $T_{\rm ex}$ derived based on equation (1), we calculated the optical depth of the ^{13}CO line as a function of the coordinates and velocity as

$$\tau_{^{13}{\rm CO}}(\alpha, \delta, V) = -\ln\left\{1 - \frac{T_{^{13}{\rm CO}}}{5.29[J(T_{\rm ex}) - 0.164]}\right\}, \tag{2}$$

where $T_{^{13}{\rm CO}}$ is the brightness temperature of the ^{13}CO line and $J(T_{\rm ex}) = 5.29/\{\exp(5.29/T_{\rm ex}) - 1\}$. We calculated the ^{13}CO column density as

$$N_{^{13}{\rm CO}}(\alpha, \delta) = 2.42 \times 10^{14}\left[\frac{T_{\rm ex}\int \tau_{^{13}{\rm CO}} dV}{1 - \exp(-5.29/T_{\rm ex})}\right] {\rm cm}^{-2}. \tag{3}$$

The total molecular column density can be estimated as $N({\rm H_2}) = 5 \times 10^5 N_{^{13}{\rm CO}}$ (Dickman 1978).

We estimated the radius of each core assuming that the cores are spherical as

$$R_{\rm core} = \sqrt{S/\pi}, \tag{4}$$

where S is the projected area of the core. The mass of each core was derived based on the following equation:

$$M_{\rm LTE} = \mu m_{\rm H} \Sigma N({\rm H_2}) \Delta x^2, \tag{5}$$

where μ is the mean molecular weight 2.8, $m_{\rm H}$ is the proton mass, and Δx^2 ($= 7''.5 \times 7''.5 \simeq 3.5 \times 10^{33}$ cm^2 at 532 pc) is the pixel size. The summation was performed over each core within the boundary. Based on the mass and radius derived above, we estimated the mean molecular number density of the cores as

$$n = \frac{3 M_{\rm LTE}}{4\pi R_{\rm core}^3 \mu m_{\rm H}}\ {\rm H_2\ cm^{-3}}. \tag{6}$$

As we discuss in the next subsection, virial masses are useful to investigate the gravitational stability of the cores. We estimated the virial mass of each core as

$$M_{\rm vir} = \frac{3a^{-1} R_{\rm core} \Delta V_{\rm comp}^2}{8(\ln 2) G}, \tag{7}$$

where G is the gravitational constant and a is the shape factor taken to be 3/5 corresponding to a centrally condensed density distribution with $\rho \propto r^{-2}$ (Bertoldi & McKee 1992). $\Delta V_{\rm comp}$ is the line width defined at full width at half-maximum of the composite spectrum averaged over each core, which we measured by a Gaussian fit. We further estimated the virial ratio $\alpha_{\rm vir}$ which is the ratio of the virial mass to the core mass, i.e.,

$$\alpha_{\rm vir} = \frac{3a^{-1} R_{\rm core} \Delta V_{\rm comp}^2}{8(\ln 2) G M_{\rm LTE}}. \tag{8}$$

In table 2, we list the identified 337 cores in order of right ascension (J2000.0) and present their physical properties derived in the above. Figure 8 shows their locations. The radius of the identified cores ranges from 0.029 to 0.180 pc

Table 2. Properties of identified cores using dendrogram.

ID	RA	Dec	$R_{\rm core}$ [pc]	$T_{\rm peak}$ [K]	Background level [K]	ΔV [km s^{-1}]	$M_{\rm vir}$ [$M_{\odot}$]	$\Sigma N(\mathrm{H_2})$ [$\times\ 10^{23}$ cm^{-2}]	$M_{\rm LTE}$ [$M_{\odot}$]	n [$\times 10^4$ cm^{-3}]	$M_{\rm vir}/M_{\rm LTE}$ ($= \alpha_{\rm vir}$)
1	$4^{\rm h}29^{\rm m}08\overset{\rm s}{.}31$	$35^{\circ}24'16\overset{''}{.}9$	0.081	9.902	**7.2**	0.654	7.23	5.41	4.50	2.92	1.61
2	$4^{\rm h}29^{\rm m}10\overset{\rm s}{.}89$	$35^{\circ}26'04\overset{''}{.}6$	0.084	10.427	**7.2**	0.641	7.20	6.31	5.24	3.05	1.37
3	$4^{\rm h}29^{\rm m}13\overset{\rm s}{.}79$	$35^{\circ}27'24\overset{''}{.}8$	0.070	9.326	**8.7**	0.606	5.37	3.90	3.25	3.26	1.65
4	$4^{\rm h}29^{\rm m}14\overset{\rm s}{.}52$	$35^{\circ}24'56\overset{''}{.}3$	0.039	11.014	**7.4**	0.806	5.35	1.90	1.58	9.19	3.38
5	$4^{\rm h}29^{\rm m}16\overset{\rm s}{.}28$	$35^{\circ}24'32\overset{''}{.}5$	0.045	11.565	**8.5**	0.771	5.59	2.47	2.06	7.77	2.72
6	$4^{\rm h}29^{\rm m}21\overset{\rm s}{.}85$	$35^{\circ}29'16\overset{''}{.}6$	0.138	8.884	**12.5**	0.631	11.50	9.09	7.55	0.99	1.52
7	$4^{\rm h}29^{\rm m}21\overset{\rm s}{.}91$	$35^{\circ}23'55\overset{''}{.}1$	0.107	12.869	**6.7**	0.927	19.20	20.57	17.10	4.81	1.12
8	$4^{\rm h}29^{\rm m}23\overset{\rm s}{.}88$	$35^{\circ}12'43\overset{''}{.}8$	0.076	9.913	**6.9**	1.194	22.78	8.52	7.09	5.56	3.21
9	$4^{\rm h}29^{\rm m}25\overset{\rm s}{.}93$	$35^{\circ}22'13\overset{''}{.}9$	0.085	7.091	**8.3**	2.237	88.42	10.93	9.09	5.10	9.73
10	$4^{\rm h}29^{\rm m}28\overset{\rm s}{.}53$	$35^{\circ}10'41\overset{''}{.}1$	0.041	9.472	**7.7**	1.394	16.59	2.77	2.30	11.51	7.20
11	$4^{\rm h}29^{\rm m}28\overset{\rm s}{.}79$	$35^{\circ}12'02\overset{''}{.}6$	0.083	11.632	**12.6**	1.032	18.52	11.34	9.43	5.68	1.96
12	$4^{\rm h}29^{\rm m}29\overset{\rm s}{.}02$	$35^{\circ}26'12\overset{''}{.}9$	0.048	10.872	**7.2**	0.785	6.12	2.83	2.35	7.33	2.60
13	$4^{\rm h}29^{\rm m}29\overset{\rm s}{.}91$	$35^{\circ}29'11\overset{''}{.}9$	0.083	9.651	**10.1**	0.625	6.78	5.36	4.45	2.68	1.52
14	$4^{\rm h}29^{\rm m}30\overset{\rm s}{.}77$	$35^{\circ}10'32\overset{''}{.}8$	0.036	10.440	**6.7**	1.351	13.82	1.64	1.37	10.10	10.11
15	$4^{\rm h}29^{\rm m}31\overset{\rm s}{.}86$	$35^{\circ}34'07\overset{''}{.}5$	0.117	9.092	**7.0**	0.764	14.21	10.83	9.00	1.94	1.58
16	$4^{\rm h}29^{\rm m}33\overset{\rm s}{.}39$	$35^{\circ}11'03\overset{''}{.}2$	0.046	12.202	**21.4**	1.477	21.13	4.60	3.83	13.55	5.52
17	$4^{\rm h}29^{\rm m}33\overset{\rm s}{.}66$	$35^{\circ}20'48\overset{''}{.}5$	0.049	7.501	**10.2**	1.732	30.60	3.40	2.83	8.27	10.83
18	$4^{\rm h}29^{\rm m}34\overset{\rm s}{.}59$	$35^{\circ}26'14\overset{''}{.}9$	0.059	12.129	**14.1**	0.723	6.43	3.28	2.72	4.57	2.36
19	$4^{\rm h}29^{\rm m}36\overset{\rm s}{.}27$	$35^{\circ}29'42\overset{''}{.}4$	0.058	10.870	**9.9**	0.730	6.43	2.33	1.93	3.42	3.32
20	$4^{\rm h}29^{\rm m}36\overset{\rm s}{.}63$	$35^{\circ}11'36\overset{''}{.}3$	0.046	14.930	**8.4**	1.197	13.86	4.26	3.54	12.53	3.92
21	$4^{\rm h}29^{\rm m}37\overset{\rm s}{.}90$	$35^{\circ}18'11\overset{''}{.}3$	0.046	11.480	**9.5**	1.539	22.93	4.24	3.52	12.47	6.51
22	$4^{\rm h}29^{\rm m}37\overset{\rm s}{.}97$	$35^{\circ}19'02\overset{''}{.}0$	0.029	11.610	**10.3**	1.454	12.76	1.97	1.64	23.14	7.79
23	$4^{\rm h}29^{\rm m}38\overset{\rm s}{.}88$	$35^{\circ}10'13\overset{''}{.}1$	0.093	12.443	**10.1**	1.355	35.56	15.98	13.28	5.69	2.68
24	$4^{\rm h}29^{\rm m}39\overset{\rm s}{.}62$	$35^{\circ}12'04\overset{''}{.}7$	0.061	16.927	**7.3**	1.263	20.27	9.24	7.68	11.66	2.64
25	$4^{\rm h}29^{\rm m}40\overset{\rm s}{.}72$	$35^{\circ}26'06\overset{''}{.}7$	0.045	16.644	**7.9**	0.734	5.07	2.47	2.06	7.77	2.47
26	$4^{\rm h}29^{\rm m}40\overset{\rm s}{.}79$	$35^{\circ}20'29\overset{''}{.}7$	0.049	13.861	**8.8**	1.809	33.40	5.86	4.87	14.27	6.86
27	$4^{\rm h}29^{\rm m}41\overset{\rm s}{.}10$	$35^{\circ}25'37\overset{''}{.}2$	0.031	18.576	**16.7**	0.702	3.18	1.18	0.98	11.38	3.23
28	$4^{\rm h}29^{\rm m}41\overset{\rm s}{.}38$	$35^{\circ}17'19\overset{''}{.}8$	0.035	15.291	**21.5**	1.451	15.19	3.73	3.10	24.93	4.90
29	$4^{\rm h}29^{\rm m}42\overset{\rm s}{.}28$	$35^{\circ}13'21\overset{''}{.}9$	0.041	13.420	**18.6**	0.996	8.46	3.27	2.72	13.59	3.11
30	$4^{\rm h}29^{\rm m}42\overset{\rm s}{.}37$	$35^{\circ}28'37\overset{''}{.}4$	0.151	10.634	**14.2**	0.851	22.88	20.65	17.17	1.72	1.33
31	$4^{\rm h}29^{\rm m}42\overset{\rm s}{.}69$	$35^{\circ}11'49\overset{''}{.}1$	0.036	15.037	**17.5**	1.503	17.10	3.35	2.78	20.54	6.15
32	$4^{\rm h}29^{\rm m}42\overset{\rm s}{.}79$	$35^{\circ}20'00\overset{''}{.}2$	0.053	14.520	**6.3**	1.390	21.60	5.92	4.92	11.39	4.39
33	$4^{\rm h}29^{\rm m}42\overset{\rm s}{.}87$	$35^{\circ}08'45\overset{''}{.}9$	0.075	10.315	**6.7**	1.308	26.75	8.95	7.44	6.08	3.59
34	$4^{\rm h}29^{\rm m}44\overset{\rm s}{.}23$	$35^{\circ}19'42\overset{''}{.}1$	0.039	15.492	**6.8**	1.207	11.98	3.11	2.59	15.04	4.63
35	$4^{\rm h}29^{\rm m}44\overset{\rm s}{.}84$	$35^{\circ}12'36\overset{''}{.}8$	0.045	20.065	**7.3**	1.346	17.05	6.45	5.37	20.29	3.18
36	$4^{\rm h}29^{\rm m}46\overset{\rm s}{.}04$	$35^{\circ}15'23\overset{''}{.}0$	0.036	18.660	**12.2**	1.259	12.00	4.44	3.69	27.27	3.25
37	$4^{\rm h}29^{\rm m}48\overset{\rm s}{.}27$	$35^{\circ}12'37\overset{''}{.}9$	0.036	21.076	**10.4**	1.638	20.29	5.85	4.86	35.88	4.18
38	$4^{\rm h}29^{\rm m}48\overset{\rm s}{.}66$	$35^{\circ}13'14\overset{''}{.}1$	0.039	21.673	**8.1**	1.352	15.03	7.09	5.89	34.23	2.55

Table 2. (Continued)

ID	RA	Dec	$R_{\rm core}$ [pc]	$T_{\rm peak}$ [K]	Background level [K]	ΔV [km s^{-1}]	$M_{\rm vir}$ [$M_\odot$]	$\Sigma N(H_2)$ [$\times 10^{23}$ cm^{-2}]	$M_{\rm LTE}$ [$M_\odot$]	n [$\times 10^4$ cm^{-3}]	$M_{\rm vir}/M_{\rm LTE}$ ($=\alpha_{\rm vir}$)
39	$4^{h}29^{m}48^{s}.73$	35°26′50.″3	0.118	13.542	**10.2**	0.664	10.88	13.00	10.81	2.27	1.01
40	$4^{h}29^{m}49^{s}.15$	35°15′29.″9	0.045	26.501	**8.3**	1.135	12.12	11.07	9.20	34.80	1.32
41	$4^{h}29^{m}49^{s}.27$	35°11′38.″3	0.050	13.723	**8.7**	1.892	37.43	6.69	5.56	15.34	6.73
42	$4^{h}29^{m}50^{s}.52$	35°12′56.″7	0.035	23.538	**7.3**	1.613	18.77	5.76	4.79	38.48	3.92
43	$4^{h}29^{m}51^{s}.41$	35°15′24.″9	0.039	30.578	**13.6**	1.223	12.30	7.61	6.32	36.72	1.95
44	$4^{h}29^{m}51^{s}.60$	35°28′20.″4	0.044	10.939	**9.2**	0.722	4.75	1.59	1.32	5.36	3.59
45	$4^{h}29^{m}53^{s}.47$	35°13′03.″5	0.049	25.132	**20.1**	1.504	23.08	11.57	9.61	28.16	2.40
46	$4^{h}29^{m}54^{s}.33$	35°11′23.″4	0.056	15.220	**27.6**	1.390	22.48	7.54	6.27	12.30	3.59
47	$4^{h}29^{m}54^{s}.35$	35°17′23.″9	0.036	15.341	**7.3**	1.327	13.32	3.04	2.53	18.66	5.27
48	$4^{h}29^{m}55^{s}.27$	35°15′46.″5	0.035	26.291	**6.8**	1.730	21.60	7.62	6.34	50.93	3.41
49	$4^{h}29^{m}55^{s}.28$	35°14′05.″0	0.042	29.807	**7.5**	1.444	18.42	12.30	10.22	47.54	1.80
50	$4^{h}29^{m}57^{s}.75$	35°14′08.″7	0.031	30.101	**12.5**	1.523	14.97	7.46	6.20	71.73	2.41
51	$4^{h}29^{m}57^{s}.77$	35°12′26.″7	0.039	20.297	**11.5**	1.249	12.84	4.92	4.09	23.75	3.14
52	$4^{h}29^{m}59^{s}.74$	35°14′08.″5	0.035	23.588	**12.1**	2.320	38.83	9.69	8.05	64.71	4.82
53	$4^{h}30^{m}00^{s}.79$	35°09′10.″5	0.084	12.872	**11.6**	1.244	27.11	13.24	11.01	6.40	2.46
54	$4^{h}30^{m}01^{s}.24$	35°13′04.″9	0.038	21.199	**13.2**	1.506	17.93	6.08	5.05	31.73	3.55
55	$4^{h}30^{m}02^{s}.98$	35°11′52.″6	0.084	19.118	**10.2**	1.436	36.13	26.57	22.09	12.84	1.64
56	$4^{h}30^{m}03^{s}.98$	35°13′37.″0	0.036	30.040	**9.9**	1.501	17.05	11.76	9.77	72.18	1.74
57	$4^{h}30^{m}04^{s}.30$	35°07′25.″4	0.031	11.178	**8.6**	1.853	22.16	2.13	1.77	20.49	12.51
58	$4^{h}30^{m}04^{s}.56$	35°07′57.″4	0.046	13.123	**8.5**	1.443	20.17	4.43	3.68	13.04	5.48
59	$4^{h}30^{m}05^{s}.01$	35°09′59.″5	0.050	14.954	**9.8**	1.304	17.79	6.46	5.37	14.80	3.31
60	$4^{h}30^{m}05^{s}.70$	35°38′10.″9	0.039	8.183	**10.1**	1.206	11.95	1.53	1.27	7.37	9.42
61	$4^{h}30^{m}05^{s}.78$	35°10′31.″1	0.046	17.389	**8.9**	1.285	15.99	6.34	5.27	18.65	3.03
62	$4^{h}30^{m}06^{s}.29$	35°11′24.″5	0.031	21.277	**7.9**	1.490	14.32	4.57	3.80	43.90	3.77
63	$4^{h}30^{m}06^{s}.73$	35°13′30.″7	0.038	28.752	**9.8**	1.797	25.52	13.64	11.34	71.21	2.25
64	$4^{h}30^{m}06^{s}.95$	35°15′50.″1	0.079	8.542	**13.5**	1.549	39.45	7.67	6.38	4.46	6.19
65	$4^{h}30^{m}07^{s}.12$	35°39′05.″3	0.075	8.386	**13.3**	1.350	28.51	7.11	5.91	4.82	4.83
66	$4^{h}30^{m}08^{s}.14$	35°07′51.″7	0.060	12.750	**10.0**	1.497	28.02	7.42	6.17	9.84	4.54
67	$4^{h}30^{m}08^{s}.37$	35°13′04.″0	0.035	27.904	**24.1**	1.736	21.75	9.17	7.62	61.23	2.85
68	$4^{h}30^{m}08^{s}.98$	35°11′11.″5	0.035	22.539	**14.4**	1.225	10.82	4.63	3.85	30.91	2.81
69	$4^{h}30^{m}09^{s}.35$	35°40′53.″6	0.082	8.071	**8.4**	1.217	25.27	6.26	5.21	3.25	4.85
70	$4^{h}30^{m}10^{s}.16$	35°11′28.″2	0.036	24.189	**7.8**	1.252	11.87	6.03	5.01	36.99	2.37
71	$4^{h}30^{m}10^{s}.82$	35°13′36.″3	0.036	24.038	**6.8**	1.801	24.53	9.65	8.02	59.23	3.06
72	$4^{h}30^{m}10^{s}.95$	35°28′46.″2	0.044	6.260	**8.3**	1.907	33.18	2.64	2.20	8.89	15.10
73	$4^{h}30^{m}10^{s}.95$	35°28′54.″7	0.049	6.364	**8.4**	1.871	35.73	2.94	2.44	7.16	14.62
74	$4^{h}30^{m}11^{s}.21$	35°37′49.″8	0.079	8.293	**9.0**	1.346	30.07	5.64	4.69	3.28	6.41
75	$4^{h}30^{m}12^{s}.19$	35°10′03.″6	0.060	19.816	**7.6**	1.520	28.86	13.42	11.16	17.80	2.59
76	$4^{h}30^{m}12^{s}.46$	35°14′59.″8	0.035	14.930	**7.9**	1.405	14.25	26.03	2.16	17.39	6.59

Table 2. (Continued)

ID	RA	Dec	R_{core} [pc]	T_{peak} [K]	Background level [K]	ΔV [km s^{-1}]	M_{vir} [$M_\odot$]	$\Sigma N(H_2)$ [× 10^{23} cm^{-2}]	M_{LTE} [$M_\odot$]	n [×10^4 cm^{-3}]	M_{vir}/M_{LTE} (= α_{vir})
77	$4^h30^m12^s.65$	$35^\circ12'20''.0$	0.064	27.389	**9.1**	1.431	27.24	22.66	18.83	24.75	1.45
78	$4^h30^m12^s.74$	$35^\circ13'06''.0$	0.044	25.186	**8.3**	1.510	20.81	10.58	8.79	35.56	2.37
79	$4^h30^m12^s.77$	$35^\circ10'51''.9$	0.029	20.927	**9.5**	1.265	9.66	2.90	2.41	34.09	4.00
80	$4^h30^m13^s.03$	$35^\circ28'07''.7$	0.036	9.217	**9.4**	1.540	17.95	1.71	1.42	10.48	12.65
81	$4^h30^m13^s.03$	$35^\circ09'26''.3$	0.038	18.273	**12.7**	1.406	15.62	3.93	3.26	20.50	4.79
82	$4^h30^m13^s.56$	$35^\circ08'13''.5$	0.045	14.564	**17.0**	1.484	20.70	5.12	4.26	16.09	4.86
83	$4^h30^m13^s.86$	$35^\circ07'23''.8$	0.049	14.247	**10.6**	1.546	24.39	5.22	4.34	12.72	5.62
84	$4^h30^m14^s.42$	$35^\circ17'44''.9$	0.036	11.829	**8.7**	1.648	20.54	3.38	2.81	20.73	7.32
85	$4^h30^m14^s.55$	$35^\circ11'28''.8$	0.033	22.923	**9.8**	1.491	15.22	6.13	5.10	48.88	2.99
86	$4^h30^m14^s.56$	$35^\circ14'45''.9$	0.038	15.206	**7.7**	1.251	12.36	3.01	2.50	15.72	4.94
87	$4^h30^m14^s.64$	$35^\circ22'54''.5$	0.051	18.552	**10.7**	1.084	12.58	7.71	6.41	16.65	1.96
88	$4^h30^m15^s.02$	$35^\circ09'14''.2$	0.033	16.840	**10.0**	1.344	12.37	3.54	2.94	28.21	4.20
89	$4^h30^m15^s.10$	$35^\circ27'58''.7$	0.064	9.347	**9.1**	1.194	18.97	4.46	3.71	4.87	5.11
90	$4^h30^m15^s.43$	$35^\circ15'31''.4$	0.038	16.910	**11.4**	1.134	10.17	2.12	1.76	11.04	5.78
91	$4^h30^m15^s.73$	$35^\circ19'41''.1$	0.033	10.684	**19.7**	1.155	9.12	1.46	1.21	11.60	7.54
92	$4^h30^m16^s.28$	$35^\circ17'05''.8$	0.057	9.337	**15.3**	2.298	62.62	9.93	8.25	15.35	7.59
93	$4^h30^m16^s.31$	$35^\circ16'08''.5$	0.052	17.916	**15.4**	1.335	19.49	9.82	8.16	19.99	2.39
94	$4^h30^m16^s.32$	$35^\circ10'26''.1$	0.035	19.474	**16.9**	1.463	15.45	4.08	3.39	27.28	4.55
95	$4^h30^m16^s.37$	$35^\circ21'09''.9$	0.036	16.383	**9.7**	1.095	9.08	2.90	2.41	17.80	3.77
96	$4^h30^m16^s.67$	$35^\circ08'29''.0$	0.044	14.883	**8.0**	1.623	24.04	4.95	4.11	16.63	5.85
97	$4^h30^m16^s.85$	$35^\circ22'17''.8$	0.069	18.419	**6.6**	1.385	27.68	15.88	13.20	13.84	2.10
98	$4^h30^m17^s.52$	$35^\circ23'33''.9$	0.058	15.514	**8.8**	1.168	16.46	7.52	6.25	11.04	2.63
99	$4^h30^m17^s.76$	$35^\circ26'53''.8$	0.059	11.345	**9.2**	1.005	12.40	4.85	4.03	6.76	3.08
100	$4^h30^m17^s.77$	$35^\circ18'12''.2$	0.048	15.137	**9.8**	1.113	12.33	4.47	3.72	11.59	3.31
101	$4^h30^m18^s.66$	$35^\circ21'44''.6$	0.044	18.353	**8.6**	1.230	13.80	4.77	3.97	16.05	3.48
102	$4^h30^m18^s.81$	$35^\circ10'57''.3$	0.039	17.607	**9.6**	1.484	18.12	5.03	4.18	24.27	4.34
103	$4^h30^m18^s.82$	$35^\circ12'50''.4$	0.049	22.454	**12.5**	1.397	19.90	11.28	9.38	27.47	2.12
104	$4^h30^m19^s.36$	$35^\circ24'32''.3$	0.035	14.961	**12.0**	1.191	10.24	2.76	2.30	18.45	4.46
105	$4^h30^m19^s.68$	$35^\circ19'07''.5$	0.042	19.443	**9.7**	0.995	8.75	5.30	4.41	20.50	1.98
106	$4^h30^m19^s.73$	$35^\circ25'40''.8$	0.062	14.287	**12.5**	0.971	12.18	7.71	6.41	9.27	1.90
107	$4^h30^m20^s.00$	$35^\circ22'57''.6$	0.038	19.563	**9.2**	1.094	9.47	3.08	2.56	16.06	3.70
108	$4^h30^m20^s.21$	$35^\circ24'00''.7$	0.042	15.874	**8.7**	1.380	16.84	3.99	3.32	15.43	5.08
109	$4^h30^m20^s.45$	$35^\circ21'03''.4$	0.042	16.688	**9.5**	1.123	11.15	3.78	3.14	14.61	3.55
110	$4^h30^m20^s.57$	$35^\circ27'51''.4$	0.041	10.530	**8.7**	1.292	14.25	2.07	1.72	8.58	8.30
111	$4^h30^m20^s.91$	$35^\circ15'52''.6$	0.058	19.488	**8.8**	1.255	19.02	8.34	6.93	12.24	2.75
112	$4^h30^m20^s.92$	$35^\circ10'01''.7$	0.042	15.330	**11.9**	1.763	27.47	6.03	5.02	23.32	5.48
113	$4^h30^m21^s.10$	$35^\circ07'47''.8$	0.045	10.029	**12.4**	2.544	60.90	5.84	4.86	18.37	12.53

Table 2. (Continued)

ID	RA	Dec	R_{core} [pc]	T_{peak} [K]	Background level [K]	ΔV [km s^{-1}]	M_{vir} [$M_\odot$]	$\Sigma N(H_2)$ [$\times 10^{23}$ cm^{-2}]	M_{LTE} [$M_\odot$]	n [$\times 10^4$ cm^{-3}]	M_{vir}/M_{LTE} (= α_{vir})
114	4h30m21.s58	35°19′42.″5	0.036	22.435	**22.5**	1.044	8.25	3.90	3.24	23.91	2.55
115	4h30m22.s32	35°10′31.″7	0.031	16.278	**8.9**	1.565	15.80	2.91	2.42	27.95	6.54
116	4h30m22.s96	35°11′49.″4	0.039	16.551	**8.3**	1.468	17.74	4.49	3.73	21.67	4.76
117	4h30m23.s17	35°12′51.″9	0.031	19.481	**8.3**	1.954	24.64	4.41	3.67	42.41	6.72
118	4h30m23.s60	35°20′29.″1	0.051	18.533	**8.3**	1.064	12.11	5.96	4.96	12.87	2.44
119	4h30m23.s61	35°21′41.″1	0.035	9.559	**8.9**	1.444	15.03	2.06	1.71	13.77	8.77
120	4h30m24.s21	35°19′42.″9	0.042	22.101	**8.7**	0.746	4.92	4.00	3.32	15.46	1.48
121	4h30m24.s35	35°41′53.″8	0.057	8.940	**9.8**	1.396	23.10	4.14	3.44	6.40	6.72
122	4h30m24.s39	35°35′23.″5	0.055	10.984	**9.2**	1.346	20.66	5.21	4.33	8.98	4.77
123	4h30m24.s52	35°27′07.″1	0.088	10.867	**13.4**	1.854	63.24	15.46	12.85	6.50	4.92
124	4h30m24.s52	35°28′58.″8	0.056	9.689	**8.6**	1.235	17.75	4.40	3.66	7.18	4.85
125	4h30m24.s54	35°08′49.″5	0.052	10.486	**17.6**	2.163	51.17	5.73	4.76	11.68	10.74
126	4h30m24.s67	35°11′12.″1	0.036	14.144	**10.0**	1.774	23.81	4.00	3.32	24.55	7.16
127	4h30m25.s30	35°10′27.″0	0.036	14.542	**7.1**	1.834	25.46	4.41	3.67	27.10	6.94
128	4h30m25.s32	35°14′31.″8	0.108	13.853	**7.6**	2.015	91.26	42.62	35.43	9.69	2.58
129	4h30m25.s46	35°42′46.″8	0.062	8.566	**8.0**	2.102	57.05	6.67	5.54	8.02	10.29
130	4h30m25.s63	35°06′41.″0	0.075	10.469	**12.8**	1.913	57.22	11.64	9.67	7.90	5.92
131	4h30m26.s13	35°39′47.″7	0.180	8.222	**16.3**	1.467	81.18	35.65	29.63	1.75	2.74
132	4h30m26.s13	35°25′45.″2	0.067	13.191	**19.4**	1.813	46.23	10.42	8.66	9.93	5.34
133	4h30m26.s23	35°08′25.″4	0.029	9.555	**19.5**	2.197	29.14	1.76	1.46	20.67	19.92
134	4h30m26.s79	35°23′37.″8	0.033	10.833	**13.3**	1.561	16.68	2.15	1.79	17.17	9.31
135	4h30m26.s91	35°45′23.″0	0.085	9.890	**27.9**	1.891	63.23	12.27	10.20	5.72	6.20
136	4h30m27.s00	35°13′37.″4	0.035	14.965	**13.2**	2.674	51.60	6.81	5.66	45.50	9.11
137	4h30m27.s26	35°26′58.″5	0.033	11.358	**8.6**	1.937	25.67	2.19	1.82	17.42	14.13
138	4h30m27.s75	35°07′46.″2	0.049	10.632	**8.1**	1.637	27.34	4.49	3.73	10.93	7.33
139	4h30m27.s93	35°21′56.″7	0.074	11.993	**9.9**	1.287	25.64	10.02	8.33	7.08	3.08
140	4h30m28.s46	35°44′58.″6	0.038	9.849	**16.9**	1.927	29.34	3.00	2.49	15.64	11.78
141	4h30m28.s67	35°10′48.″2	0.053	12.905	**12.0**	2.248	56.49	8.45	7.02	16.25	8.04
142	4h30m28.s92	35°09′09.″7	0.045	11.684	**16.3**	2.419	55.06	7.52	6.25	23.63	8.81
143	4h30m29.s16	35°44′27.″4	0.049	9.907	**9.1**	1.923	37.72	4.64	3.86	11.29	9.78
144	4h30m29.s35	35°30′36.″5	0.050	9.199	**18.0**	1.226	15.70	2.18	1.81	4.99	8.68
145	4h30m29.s38	35°26′24.″7	0.046	11.453	**8.4**	1.942	36.51	4.90	4.07	14.41	8.97
146	4h30m29.s52	35°29′02.″4	0.068	9.168	**18.5**	1.525	33.15	5.02	4.17	4.57	7.94
147	4h30m30.s26	35°19′36.″6	0.038	11.686	**8.8**	1.189	11.16	2.40	1.99	12.52	5.60
148	4h30m30.s38	35°05′59.″6	0.048	11.119	**8.0**	2.249	50.29	5.60	4.66	14.50	10.80
149	4h30m30.s42	35°07′12.″4	0.049	9.265	**10.6**	1.912	37.30	4.47	3.72	10.89	10.03
150	4h30m30.s79	35°34′26.″7	0.044	12.141	**7.8**	1.508	20.74	4.39	3.65	14.76	5.68

Table 2. (Continued)

ID	RA	Dec	$R_{\rm core}$ [pc]	$T_{\rm peak}$ [K]	Background level [K]	ΔV [km s^{-1}]	$M_{\rm vir}$ [$M_\odot$]	$\Sigma N({\rm H_2})$ [× 10^{23} cm^{-2}]	$M_{\rm LTE}$ [$M_\odot$]	n [×10^4 cm^{-3}]	$M_{\rm vir}/M_{\rm LTE}$ (= $\alpha_{\rm vir}$)
151	$4^h30^m30^s.88$	35°25′59″.4	0.029	10.336	**9.6**	1.748	18.44	1.45	1.21	17.08	15.25
152	$4^h30^m30^s.89$	35°12′38″.2	0.045	12.159	**7.6**	2.349	51.91	6.20	5.16	19.50	10.07
153	$4^h30^m30^s.99$	35°08′32″.1	0.060	10.630	**8.2**	1.928	46.45	5.81	4.83	7.70	9.63
154	$4^h30^m31^s.29$	35°19′07″.9	0.065	11.453	**7.0**	1.018	13.99	6.54	5.44	6.82	2.57
155	$4^h30^m31^s.38$	35°06′29″.6	0.055	10.740	**7.3**	2.049	47.91	7.57	6.29	13.03	7.62
156	$4^h30^m31^s.86$	35°14′23″.0	0.091	20.470	**9.0**	1.443	39.45	30.86	25.65	11.73	1.54
157	$4^h30^m32^s.15$	35°43′19″.8	0.046	9.973	**12.4**	1.794	31.17	4.05	3.36	11.91	9.27
158	$4^h30^m32^s.36$	35°21′44″.3	0.048	12.252	**7.5**	0.994	9.82	4.06	3.38	10.53	2.91
159	$4^h30^m33^s.28$	35°20′28″.5	0.068	11.756	**13.2**	1.535	33.56	8.02	6.66	7.30	5.04
160	$4^h30^m33^s.33$	35°25′25″.7	0.045	10.792	**9.9**	1.543	22.38	3.57	2.97	11.23	7.53
161	$4^h30^m33^s.53$	35°26′28″.3	0.035	10.357	**10.7**	1.499	16.22	2.04	1.70	13.64	9.56
162	$4^h30^m33^s.58$	35°07′49″.9	0.042	10.671	**18.9**	1.498	19.83	2.74	2.28	10.61	8.69
163	$4^h30^m33^s.69$	35°10′55″.4	0.074	9.152	**14.1**	2.377	87.43	11.56	9.61	8.17	9.10
164	$4^h30^m33^s.75$	35°23′23″.0	0.035	10.358	**13.4**	1.197	10.33	1.63	1.35	10.86	7.64
165	$4^h30^m34^s.49$	35°13′57″.0	0.029	15.463	**9.3**	1.674	16.91	2.49	2.07	29.27	8.16
166	$4^h30^m34^s.88$	35°23′00″.5	0.044	11.137	**6.2**	0.945	8.14	1.95	1.62	6.57	5.01
167	$4^h30^m35^s.68$	35°37′49″.4	0.031	8.889	**8.6**	1.252	10.12	1.28	1.07	12.33	9.49
168	$4^h30^m35^s.74$	35°08′20″.4	0.050	9.444	**8.0**	1.790	33.51	4.01	3.34	9.20	10.04
169	$4^h30^m35^s.79$	35°19′27″.0	0.035	10.561	**13.2**	0.992	7.09	1.70	1.41	11.37	5.01
170	$4^h30^m35^s.91$	35°24′42″.0	0.041	7.569	**9.9**	1.666	23.68	1.92	1.60	7.99	14.81
171	$4^h30^m36^s.01$	35°18′38″.1	0.038	10.035	**8.0**	1.074	9.11	1.57	1.31	8.20	6.98
172	$4^h30^m36^s.45$	35°07′24″.1	0.065	9.690	**9.0**	1.640	36.82	7.88	6.55	8.22	5.62
173	$4^h30^m36^s.71$	35°29′56″.2	0.036	11.208	**7.2**	1.682	21.40	2.35	1.95	14.43	10.95
174	$4^h30^m36^s.76$	35°06′08″.6	0.045	12.176	**8.8**	1.413	18.79	3.95	3.28	12.41	5.72
175	$4^h30^m36^s.77$	35°35′58″.0	0.081	10.911	**6.4**	1.401	33.23	9.47	7.87	5.11	4.22
176	$4^h30^m36^s.90$	35°25′21″.0	0.044	8.889	**6.4**	1.449	19.15	2.31	1.92	7.78	9.96
177	$4^h30^m37^s.02$	35°42′45″.7	0.074	8.803	**8.1**	1.478	33.82	5.87	4.88	4.15	6.94
178	$4^h30^m37^s.12$	35°21′45″.1	0.039	10.011	**7.1**	1.490	18.27	2.27	1.88	10.94	9.70
179	$4^h30^m37^s.19$	35°23′45″.9	0.042	8.787	**11.2**	1.225	13.25	1.77	1.47	6.83	9.02
180	$4^h30^m37^s.27$	35°11′47″.5	0.038	7.545	**14.5**	2.264	40.51	2.12	1.76	11.04	23.04
181	$4^h30^m37^s.49$	35°37′30″.9	0.036	9.952	**7.1**	1.307	12.93	1.25	1.04	7.66	12.47
182	$4^h30^m37^s.72$	35°20′27″.9	0.046	9.465	**8.7**	1.424	19.63	2.50	2.08	7.35	9.46
183	$4^h30^m37^s.94$	35°18′57″.1	0.038	9.241	**9.6**	1.035	8.46	1.56	1.30	8.15	6.52
184	$4^h30^m38^s.90$	35°44′12″.3	0.045	9.080	**11.9**	1.524	21.84	2.80	2.33	8.80	9.38
185	$4^h30^m38^s.96$	35°45′23″.5	0.078	7.899	**8.2**	1.740	49.31	7.46	6.20	4.50	7.95
186	$4^h30^m38^s.99$	35°34′57″.4	0.035	11.028	**9.8**	1.485	15.91	1.95	1.62	13.05	9.80
187	$4^h30^m39^s.16$	35°08′15″.3	0.036	8.280	**15.0**	2.088	33.00	2.02	1.68	12.42	19.62
188	$4^h30^m39^s.23$	35°38′53″.2	0.048	8.514	**16.2**	1.203	14.39	2.32	1.93	6.01	7.45

Table 2. (Continued)

ID	RA	Dec	R_{core} [pc]	T_{peak} [K]	Background level [K]	ΔV [km s^{-1}]	M_{vir} [$M_\odot$]	$\Sigma N(H_2)$ [$\times 10^{23}$ cm^{-2}]	M_{LTE} [$M_\odot$]	n [$\times 10^4$ cm^{-3}]	M_{vir}/M_{LTE} ($= \alpha_{vir}$)
189	$4^h30^m39\overset{s}{.}30$	$35°14'14\overset{''}{.}8$	0.038	12.043	**16.3**	1.551	19.02	2.93	2.44	15.31	7.80
190	$4^h30^m39\overset{s}{.}33$	$35°18'12\overset{''}{.}4$	0.046	8.542	**23.8**	0.909	8.01	2.10	1.74	6.17	4.60
191	$4^h30^m39\overset{s}{.}57$	$35°22'16\overset{''}{.}4$	0.044	12.458	**8.2**	1.194	13.00	3.23	2.68	10.86	4.84
192	$4^h30^m39\overset{s}{.}74$	$35°19'30\overset{''}{.}6$	0.051	8.917	**26.2**	1.248	16.66	3.07	2.56	6.64	6.52
193	$4^h30^m40\overset{s}{.}07$	$35°06'53\overset{''}{.}4$	0.046	9.052	**28.3**	1.432	19.86	2.60	2.16	7.64	9.20
194	$4^h30^m40\overset{s}{.}09$	$35°33'44\overset{''}{.}4$	0.042	13.840	**22.9**	1.614	23.03	3.85	3.20	14.87	7.20
195	$4^h30^m40\overset{s}{.}39$	$35°05'59\overset{''}{.}9$	0.059	11.181	**7.5**	1.364	22.84	4.57	3.80	6.38	6.01
196	$4^h30^m40\overset{s}{.}52$	$35°29'21\overset{''}{.}7$	0.036	18.353	**12.4**	1.486	16.71	4.45	3.70	27.32	4.52
197	$4^h30^m40\overset{s}{.}59$	$35°27'56\overset{''}{.}0$	0.065	19.268	**9.4**	1.337	24.49	13.89	11.55	14.49	2.12
198	$4^h30^m40\overset{s}{.}66$	$35°21'37\overset{''}{.}1$	0.035	13.307	**11.1**	1.248	11.24	2.33	1.94	15.57	5.80
199	$4^h30^m40\overset{s}{.}91$	$35°35'41\overset{''}{.}0$	0.042	9.836	**10.3**	1.615	23.04	2.86	2.38	11.06	9.68
200	$4^h30^m41\overset{s}{.}30$	$35°40'51\overset{''}{.}7$	0.045	7.568	**8.2**	1.267	15.09	1.94	1.62	6.11	9.33
201	$4^h30^m41\overset{s}{.}38$	$35°28'39\overset{''}{.}4$	0.042	19.346	**6.3**	1.369	16.56	5.55	4.61	21.45	3.59
202	$4^h30^m41\overset{s}{.}40$	$35°11'33\overset{''}{.}7$	0.085	6.693	**6.9**	2.224	87.42	10.86	9.03	5.06	9.69
203	$4^h30^m41\overset{s}{.}50$	$35°31'01\overset{''}{.}9$	0.035	13.705	**7.0**	1.548	17.28	3.03	2.52	20.22	6.87
204	$4^h30^m41\overset{s}{.}59$	$35°43'09\overset{''}{.}9$	0.101	8.797	**6.4**	1.476	45.81	12.98	10.79	3.61	4.25
205	$4^h30^m41\overset{s}{.}79$	$35°08'31\overset{''}{.}7$	0.036	8.145	**8.1**	1.967	29.27	2.21	1.84	13.58	15.91
206	$4^h30^m41\overset{s}{.}80$	$35°22'44\overset{''}{.}7$	0.048	11.270	**6.7**	1.420	20.07	4.07	3.38	10.53	5.94
207	$4^h30^m42\overset{s}{.}74$	$35°36'15\overset{''}{.}5$	0.057	10.861	**6.8**	1.377	22.46	4.95	4.12	7.66	5.46
208	$4^h30^m43\overset{s}{.}21$	$35°32'30\overset{''}{.}2$	0.069	14.908	**7.2**	1.464	30.91	12.01	9.98	10.47	3.10
209	$4^h30^m43\overset{s}{.}26$	$35°21'32\overset{''}{.}7$	0.051	11.841	**9.3**	1.666	29.70	5.48	4.56	11.84	6.52
210	$4^h30^m43\overset{s}{.}31$	$35°44'16\overset{''}{.}5$	0.035	7.667	**8.7**	1.751	22.13	1.35	1.13	9.04	19.67
211	$4^h30^m43\overset{s}{.}46$	$35°25'01\overset{''}{.}0$	0.039	8.995	**7.0**	1.678	23.18	2.01	1.67	9.70	13.88
212	$4^h30^m43\overset{s}{.}59$	$35°33'55\overset{''}{.}3$	0.038	12.503	**6.9**	1.513	18.09	2.27	1.89	11.87	9.57
213	$4^h30^m43\overset{s}{.}66$	$35°38'21\overset{''}{.}4$	0.051	9.039	**7.4**	1.511	24.42	2.78	2.31	5.99	10.59
214	$4^h30^m43\overset{s}{.}74$	$35°07'00\overset{''}{.}2$	0.041	8.773	**14.2**	1.427	17.39	2.44	2.03	10.14	8.58
215	$4^h30^m43\overset{s}{.}79$	$35°24'17\overset{''}{.}1$	0.062	8.801	**13.5**	1.532	30.29	4.76	3.95	5.72	7.66
216	$4^h30^m43\overset{s}{.}99$	$35°31'03\overset{''}{.}0$	0.033	15.312	**7.7**	1.447	14.33	2.19	1.82	17.43	7.88
217	$4^h30^m44\overset{s}{.}02$	$35°29'24\overset{''}{.}4$	0.070	18.105	**10.4**	1.474	31.74	13.79	11.46	11.51	2.77
218	$4^h30^m44\overset{s}{.}10$	$35°07'54\overset{''}{.}8$	0.041	8.785	**9.8**	2.038	35.45	2.48	2.06	10.32	17.17
219	$4^h30^m44\overset{s}{.}23$	$35°35'44\overset{''}{.}0$	0.041	9.447	**13.6**	1.555	20.65	2.10	1.75	8.73	11.82
220	$4^h30^m44\overset{s}{.}67$	$35°19'32\overset{''}{.}9$	0.046	8.683	**15.0**	1.301	16.37	2.59	2.15	7.61	7.62
221	$4^h30^m45\overset{s}{.}06$	$35°14'49\overset{''}{.}4$	0.049	5.808	**17.7**	1.955	39.00	2.84	2.36	6.92	16.51
222	$4^h30^m45\overset{s}{.}20$	$35°26'21\overset{''}{.}6$	0.029	18.356	**19.8**	1.060	6.78	1.04	0.86	12.17	7.87
223	$4^h30^m45\overset{s}{.}36$	$35°34'31\overset{''}{.}5$	0.036	10.202	**19.8**	1.581	18.92	1.81	1.51	11.14	12.54
224	$4^h30^m45\overset{s}{.}40$	$35°37'03\overset{''}{.}3$	0.067	9.925	**11.3**	1.523	32.63	7.42	6.17	7.07	5.29
225	$4^h30^m45\overset{s}{.}50$	$35°31'23\overset{''}{.}1$	0.035	15.365	**9.5**	1.388	13.90	2.66	2.21	17.74	6.30
226	$4^h30^m45\overset{s}{.}56$	$35°28'37\overset{''}{.}2$	0.039	13.084	**13.0**	1.598	21.00	3.24	2.69	15.63	7.80

Table 2. (Continued)

ID	RA	Dec	$R_{\rm core}$ [pc]	$T_{\rm peak}$ [K]	Background level [K]	ΔV [km s^{-1}]	$M_{\rm vir}$ [$M_{\odot}$]	$\Sigma N({\rm H_2})$ [$\times 10^{23}$ cm^{-2}]	$M_{\rm LTE}$ [$M_{\odot}$]	n [$\times 10^4$ cm^{-3}]	$M_{\rm vir}/M_{\rm LTE}$ ($= \alpha_{\rm vir}$)
227	$4^{h}30^{m}45^{s}.60$	$35^{\circ}22'48''.3$	0.053	10.510	**11.3**	1.535	26.32	4.44	3.69	8.54	7.13
228	$4^{h}30^{m}45^{s}.76$	$35^{\circ}33'14''.2$	0.046	14.315	**8.6**	1.437	20.00	4.31	3.58	12.67	5.59
229	$4^{h}30^{m}46^{s}.11$	$35^{\circ}13'42''.5$	0.044	8.768	**9.2**	1.368	17.07	3.19	2.65	10.73	6.43
230	$4^{h}30^{m}46^{s}.17$	$35^{\circ}26'59''.3$	0.073	18.542	**15.4**	1.124	19.34	12.80	10.64	9.43	1.82
231	$4^{h}30^{m}46^{s}.34$	$35^{\circ}20'36''.6$	0.041	7.521	**8.8**	2.149	39.42	2.53	2.11	10.53	18.72
232	$4^{h}30^{m}46^{s}.81$	$35^{\circ}36'20''.0$	0.042	9.091	**9.2**	1.570	21.79	2.75	2.29	10.64	9.52
233	$4^{h}30^{m}46^{s}.83$	$35^{\circ}06'08''.7$	0.060	9.789	**14.5**	1.272	20.21	4.41	3.67	5.85	5.51
234	$4^{h}30^{m}46^{s}.98$	$35^{\circ}43'53''.3$	0.100	7.600	**11.4**	1.641	56.31	12.23	10.17	3.50	5.54
235	$4^{h}30^{m}47^{s}.14$	$35^{\circ}20'31''.2$	0.065	7.028	**10.3**	2.184	64.36	5.90	4.91	6.16	13.11
236	$4^{h}30^{m}47^{s}.43$	$35^{\circ}34'54''.4$	0.071	8.921	**9.8**	1.761	45.84	7.20	5.99	5.76	7.66
237	$4^{h}30^{m}47^{s}.45$	$35^{\circ}10'43''.7$	0.083	8.332	**6.8**	1.712	50.95	12.44	10.34	6.23	4.93
238	$4^{h}30^{m}47^{s}.57$	$35^{\circ}08'36''.8$	0.029	9.236	**8.5**	2.100	26.63	1.46	1.21	17.11	21.99
239	$4^{h}30^{m}48^{s}.12$	$35^{\circ}32'39''.8$	0.036	14.603	**10.0**	1.594	19.23	3.09	2.56	18.94	7.50
240	$4^{h}30^{m}48^{s}.15$	$35^{\circ}08'04''.0$	0.051	9.326	**13.2**	1.844	36.38	4.99	4.15	10.78	8.77
241	$4^{h}30^{m}48^{s}.58$	$35^{\circ}24'16''.8$	0.052	7.488	**9.1**	1.755	33.70	3.02	2.51	6.15	13.43
242	$4^{h}30^{m}48^{s}.63$	$35^{\circ}38'52''.2$	0.065	9.583	**12.6**	1.263	21.83	5.21	4.33	5.44	5.04
243	$4^{h}30^{m}48^{s}.84$	$35^{\circ}37'11''.3$	0.044	11.175	**8.4**	1.455	19.33	3.13	2.60	10.53	7.43
244	$4^{h}30^{m}49^{s}.36$	$35^{\circ}22'28''.2$	0.058	10.779	**8.6**	1.650	32.89	7.00	5.82	10.28	5.65
245	$4^{h}30^{m}49^{s}.62$	$35^{\circ}41'56''.8$	0.090	7.073	**8.7**	1.485	41.52	6.86	5.70	2.69	7.29
246	$4^{h}30^{m}50^{s}.33$	$35^{\circ}37'47''.0$	0.042	11.625	**8.9**	1.414	17.67	2.92	2.43	11.29	7.28
247	$4^{h}30^{m}50^{s}.65$	$35^{\circ}07'14''.2$	0.060	8.358	**20.0**	1.494	27.91	5.51	4.58	7.30	6.10
248	$4^{h}30^{m}50^{s}.83$	$35^{\circ}20'10''.2$	0.065	6.586	**12.7**	1.774	42.50	4.34	3.61	4.53	11.77
249	$4^{h}30^{m}50^{s}.94$	$35^{\circ}08'29''.5$	0.081	8.321	**6.9**	1.697	48.76	12.45	10.35	6.71	4.71
250	$4^{h}30^{m}50^{s}.94$	$35^{\circ}20'32''.8$	0.051	7.282	**19.8**	1.869	37.37	2.90	2.41	6.26	15.51
251	$4^{h}30^{m}51^{s}.53$	$35^{\circ}24'16''.9$	0.039	7.124	**15.6**	1.820	27.24	1.64	1.36	7.90	20.04
252	$4^{h}30^{m}51^{s}.67$	$35^{\circ}34'23''.0$	0.039	10.308	**10.7**	1.434	16.93	1.96	1.63	9.47	10.39
253	$4^{h}30^{m}51^{s}.82$	$35^{\circ}10'48''.9$	0.033	9.772	**8.4**	1.727	20.41	2.35	1.95	18.71	10.46
254	$4^{h}30^{m}51^{s}.93$	$35^{\circ}26'43''.7$	0.035	14.081	**11.6**	1.272	11.67	2.58	2.15	17.25	5.44
255	$4^{h}30^{m}52^{s}.21$	$35^{\circ}39'45''.6$	0.095	10.201	**10.0**	1.183	27.66	11.12	9.24	3.72	2.99
256	$4^{h}30^{m}52^{s}.21$	$35^{\circ}26'09''.0$	0.036	12.004	**10.9**	1.345	13.70	1.55	1.29	9.53	10.62
257	$4^{h}30^{m}52^{s}.36$	$35^{\circ}38'39''.5$	0.036	10.691	**11.1**	1.310	12.99	1.78	1.48	10.91	8.79
258	$4^{h}30^{m}52^{s}.39$	$35^{\circ}38'04''.3$	0.048	11.447	**8.3**	1.365	18.54	3.54	2.94	9.17	6.30
259	$4^{h}30^{m}52^{s}.60$	$35^{\circ}32'53''.2$	0.042	12.147	**8.0**	1.375	16.70	2.60	2.16	10.06	7.72
260	$4^{h}30^{m}53^{s}.21$	$35^{\circ}29'22''.5$	0.052	14.017	**16.6**	1.100	13.24	5.03	4.18	10.24	3.17
261	$4^{h}30^{m}53^{s}.37$	$35^{\circ}27'57''.9$	0.033	14.905	**14.9**	1.108	8.41	1.67	1.39	13.33	6.05
262	$4^{h}30^{m}53^{s}.83$	$35^{\circ}22'56''.0$	0.036	9.497	**6.9**	1.876	26.63	2.14	1.78	13.13	14.98
263	$4^{h}30^{m}53^{s}.88$	$35^{\circ}21'08''.6$	0.042	8.843	**10.5**	1.921	32.60	2.68	2.23	10.37	14.62
264	$4^{h}30^{m}54^{s}.23$	$35^{\circ}28'33''.9$	0.044	13.970	**16.1**	1.137	11.80	3.47	2.89	11.68	4.09

Table 2. (Continued)

ID	RA	Dec	R_{core} [pc]	T_{peak} [K]	Background level [K]	ΔV [km s^{-1}]	M_{vir} [$M_{\odot}$]	$\Sigma N(H_2)$ [× 10^{23} cm^{-2}]	M_{LTE} [$M_{\odot}$]	n [×10^4 cm^{-3}]	M_{vir}/M_{LTE} (= α_{vir})
265	4h30m54.s42	35°08′19.″6	0.041	8.073	**8.8**	1.547	20.44	2.39	1.99	9.95	10.27
266	4h30m54.s50	35°44′53.″1	0.062	6.756	**10.0**	1.397	25.17	3.48	2.90	4.19	8.69
267	4h30m54.s55	35°11′24.″8	0.068	9.768	**26.4**	1.513	32.62	7.89	6.56	7.18	4.98
268	4h30m54.s58	35°43′45.″7	0.051	7.474	**20.8**	0.941	9.47	2.29	1.90	4.94	4.98
269	4h30m54.s70	35°22′12.″7	0.041	9.185	**11.7**	1.778	27.00	2.80	2.32	11.62	11.62
270	4h30m55.s17	35°31′07.″5	0.078	12.169	**10.9**	1.311	27.98	10.38	8.63	6.27	3.24
271	4h30m55.s45	35°07′04.″4	0.067	8.420	**11.2**	1.419	28.30	6.19	5.14	5.89	5.50
272	4h30m55.s76	35°26′53.″4	0.035	10.734	**10.5**	1.110	8.90	1.53	1.27	10.20	7.01
273	4h30m55.s81	35°32′46.″0	0.041	12.242	**7.5**	1.300	14.42	3.33	2.77	13.82	5.21
274	4h30m56.s26	35°38′49.″6	0.033	11.077	**7.8**	1.243	10.58	1.57	1.31	12.55	8.08
275	4h30m56.s33	35°20′35.″4	0.085	9.266	**7.3**	1.531	41.77	10.62	8.83	4.95	4.73
276	4h30m56.s33	35°40′00.″6	0.039	11.156	**15.3**	1.067	9.36	1.94	1.62	9.38	5.79
277	4h30m56.s57	35°23′05.″8	0.038	8.810	**9.4**	1.781	25.07	2.82	2.35	14.73	10.69
278	4h30m56.s98	35°33′53.″9	0.045	9.670	**6.8**	1.763	29.24	3.43	2.85	10.79	10.25
279	4h30m57.s05	35°34′40.″6	0.046	7.312	**15.2**	2.114	43.26	3.32	2.76	9.78	15.65
280	4h30m57.s66	35°41′01.″3	0.083	10.013	**9.8**	1.123	21.92	8.32	6.91	4.17	3.17
281	4h30m57.s69	35°28′33.″4	0.057	13.166	**12.7**	1.155	15.82	4.89	4.07	7.57	3.89
282	4h30m57.s79	35°35′12.″0	0.039	6.837	**18.7**	2.247	41.54	2.03	1.68	9.79	24.66
283	4h30m58.s03	35°30′08.″9	0.036	13.325	**24.7**	1.119	9.47	2.30	1.91	14.10	4.96
284	4h30m58.s29	35°11′56.″4	0.039	12.273	**17.0**	1.220	12.25	2.63	2.19	12.69	5.61
285	4h30m59.s35	35°21′44.″9	0.041	9.347	**9.9**	1.726	25.44	2.33	1.94	9.69	13.13
286	4h31m00.s36	35°26′52.″6	0.051	9.708	**9.5**	0.953	9.72	2.65	2.20	5.72	4.42
287	4h31m00.s62	35°19′42.″1	0.033	8.452	**9.0**	1.465	14.69	1.18	0.98	9.39	15.00
288	4h31m00.s90	35°12′05.″3	0.031	10.921	**10.3**	1.917	23.70	2.30	1.91	22.15	12.38
289	4h31m02.s01	35°23′08.″4	0.045	7.861	**9.6**	1.629	24.96	2.16	1.80	6.79	13.90
290	4h31m02.s46	35°28′53.″3	0.033	10.258	**9.2**	1.399	13.39	1.59	1.32	12.68	10.12
291	4h31m03.s12	35°19′17.″1	0.070	8.346	**10.6**	1.844	49.67	7.50	6.23	6.26	7.97
292	4h31m03.s21	35°30′14.″6	0.052	10.079	**9.0**	1.187	15.41	3.52	2.93	7.17	5.26
293	4h31m03.s43	35°26′00.″1	0.051	10.470	**11.5**	0.941	9.47	3.08	2.56	6.65	3.70
294	4h31m04.s56	35°32′14.″8	0.033	11.503	**8.6**	0.834	4.76	1.27	1.05	10.11	4.52
295	4h31m04.s75	35°20′31.″6	0.105	9.009	**15.9**	1.541	51.98	13.75	11.43	3.40	4.55
296	4h31m05.s17	35°12′34.″7	0.039	10.382	**9.9**	1.982	32.31	3.89	3.24	18.79	9.99
297	4h31m07.s02	35°32′55.″6	0.044	7.798	**7.2**	1.306	15.56	1.70	1.41	5.71	11.02
298	4h31m08.s26	35°31′02.″0	0.104	8.724	**7.5**	1.203	31.51	12.35	10.27	3.14	3.07
299	4h31m08.s43	35°34′41.″6	0.097	8.127	**8.0**	1.802	65.87	12.98	10.79	4.07	6.10
300	4h31m08.s68	35°13′16.″1	0.078	8.877	**9.3**	1.574	40.37	11.34	9.43	6.84	4.28

Table 2. (Continued)

ID	RA	Dec	R_{core} [pc]	T_{peak} [K]	Background level [K]	ΔV [km s^{-1}]	M_{vir} [$M_{\odot}$]	$\Sigma N(H_2)$ [$\times 10^{23}$ cm^{-2}]	M_{LTE} [$M_{\odot}$]	n [$\times 10^4$ cm^{-3}]	M_{vir}/M_{LTE} (= α_{vir})
301	$4^{h}31^{m}09^{s}.11$	$35^{\circ}27'55''.6$	0.110	10.759	**13.9**	0.948	20.72	1.06	0.88	0.23	23.58
302	$4^{h}31^{m}09^{s}.81$	$35^{\circ}20'58''.2$	0.050	9.583	**22.8**	1.531	24.52	12.19	10.13	27.93	2.42
303	$4^{h}31^{m}10^{s}.65$	$35^{\circ}22'16''.7$	0.087	8.850	**8.4**	1.494	40.72	10.05	8.35	4.37	4.87
304	$4^{h}31^{m}11^{s}.69$	$35^{\circ}23'29''.5$	0.055	8.274	**20.7**	1.264	18.23	3.54	2.94	6.09	6.20
305	$4^{h}31^{m}12^{s}.10$	$35^{\circ}19'05''.6$	0.036	7.070	**6.8**	1.535	17.83	1.14	0.95	7.03	18.74
306	$4^{h}31^{m}12^{s}.53$	$35^{\circ}20'33''.4$	0.046	9.021	**8.0**	1.358	17.84	2.96	2.46	8.71	7.25
307	$4^{h}31^{m}13^{s}.69$	$35^{\circ}26'29''.5$	0.041	9.950	**8.2**	0.763	4.97	1.56	1.30	6.50	3.82
308	$4^{h}31^{m}13^{s}.69$	$35^{\circ}42'35''.8$	0.049	8.014	**8.7**	0.821	6.87	1.32	1.10	3.21	6.27
309	$4^{h}31^{m}13^{s}.87$	$35^{\circ}22'59''.5$	0.062	9.619	**9.1**	1.323	22.59	5.29	4.39	6.35	5.14
310	$4^{h}31^{m}14^{s}.43$	$35^{\circ}43'54''.6$	0.085	8.250	**11.2**	0.864	13.30	5.32	4.42	2.48	3.01
311	$4^{h}31^{m}14^{s}.90$	$35^{\circ}25'11''.2$	0.125	10.704	**13.2**	1.123	32.92	19.44	16.16	2.85	2.04
312	$4^{h}31^{m}16^{s}.05$	$35^{\circ}09'47''.7$	0.049	7.764	**14.1**	1.203	14.77	2.99	2.48	7.27	5.95
313	$4^{h}31^{m}18^{s}.44$	$35^{\circ}24'04''.4$	0.063	10.372	**12.9**	1.135	16.90	4.46	3.71	5.11	4.56
314	$4^{h}31^{m}19^{s}.53$	$35^{\circ}29'28''.0$	0.048	8.903	**17.8**	1.520	22.98	2.84	2.36	7.37	9.72
315	$4^{h}31^{m}20^{s}.77$	$35^{\circ}21'24''.6$	0.084	7.095	**8.1**	1.686	49.82	8.00	6.65	3.86	7.49
316	$4^{h}31^{m}21^{s}.20$	$35^{\circ}24'47''.7$	0.041	8.865	**14.2**	1.239	13.10	2.07	1.72	8.61	7.61
317	$4^{h}31^{m}21^{s}.85$	$35^{\circ}28'30''.4$	0.105	9.758	**9.1**	0.872	16.74	8.86	7.36	2.19	2.27
318	$4^{h}31^{m}26^{s}.83$	$35^{\circ}39'07''.4$	0.166	8.183	**12.4**	1.312	59.78	32.01	26.61	2.00	2.25
319	$4^{h}31^{m}29^{s}.50$	$35^{\circ}27'35''.7$	0.060	8.265	**14.1**	0.725	6.57	2.69	2.23	3.56	2.94
320	$4^{h}31^{m}29^{s}.50$	$35^{\circ}40'31''.9$	0.033	8.758	**24.0**	1.247	10.65	1.06	0.88	8.43	12.12
321	$4^{h}31^{m}32^{s}.31$	$35^{\circ}38'42''.2$	0.046	8.066	**19.0**	1.487	21.40	2.30	1.91	6.76	11.20
322	$4^{h}31^{m}33^{s}.57$	$35^{\circ}29'29''.5$	0.070	7.412	**16.0**	1.023	15.29	4.59	3.81	3.83	4.01
323	$4^{h}31^{m}35^{s}.16$	$35^{\circ}28'02''.9$	0.078	7.827	**17.5**	0.781	9.95	4.11	3.42	2.48	2.91
324	$4^{h}31^{m}37^{s}.44$	$35^{\circ}28'34''.1$	0.065	7.833	**8.8**	0.841	9.68	3.14	2.61	3.28	3.71
325	$4^{h}31^{m}38^{s}.92$	$35^{\circ}27'34''.9$	0.057	7.083	**14.1**	1.073	13.64	1.81	1.50	2.79	9.08
326	$4^{h}31^{m}39^{s}.77$	$35^{\circ}29'20''.6$	0.063	6.621	**17.1**	1.458	27.85	3.78	3.14	4.33	8.86
327	$4^{h}31^{m}42^{s}.79$	$35^{\circ}28'04''.8$	0.059	7.204	**10.7**	1.040	13.29	2.65	2.21	3.70	6.02
328	$4^{h}31^{m}44^{s}.31$	$35^{\circ}21'24''.3$	0.109	7.320	**17.0**	1.037	24.55	7.90	6.57	1.75	3.74
329	$4^{h}31^{m}44^{s}.85$	$35^{\circ}27'05''.2$	0.071	6.944	**7.5**	1.215	21.83	4.63	3.85	3.71	5.67
330	$4^{h}31^{m}45^{s}.92$	$35^{\circ}26'35''.4$	0.042	7.403	**10.1**	1.235	13.48	1.24	1.03	4.78	13.11
331	$4^{h}31^{m}47^{s}.35$	$35^{\circ}25'40''.4$	0.098	8.399	**17.7**	0.646	8.56	5.28	4.39	1.61	1.95
332	$4^{h}31^{m}48^{s}.47$	$35^{\circ}27'28''.1$	0.078	7.050	**10.4**	0.919	13.77	5.11	4.25	3.08	3.24
333	$4^{h}31^{m}52^{s}.97$	$35^{\circ}27'58''.5$	0.065	7.961	**15.2**	0.807	8.92	2.59	2.15	2.70	4.14
334	$4^{h}31^{m}56^{s}.74$	$35^{\circ}26'11''.0$	0.042	6.883	**13.5**	0.736	4.78	1.04	0.86	4.00	5.55
335	$4^{h}31^{m}57^{s}.31$	$35^{\circ}22'54''.6$	0.098	8.141	**15.2**	0.826	14.00	6.83	5.67	2.08	2.47
336	$4^{h}31^{m}59^{s}.17$	$35^{\circ}26'58''.2$	0.085	7.054	**9.7**	0.849	12.74	3.35	2.78	1.56	4.58
337	$4^{h}32^{m}00^{s}.26$	$35^{\circ}22'05''.1$	0.117	7.576	**7.7**	1.088	28.86	10.32	8.58	1.85	3.36

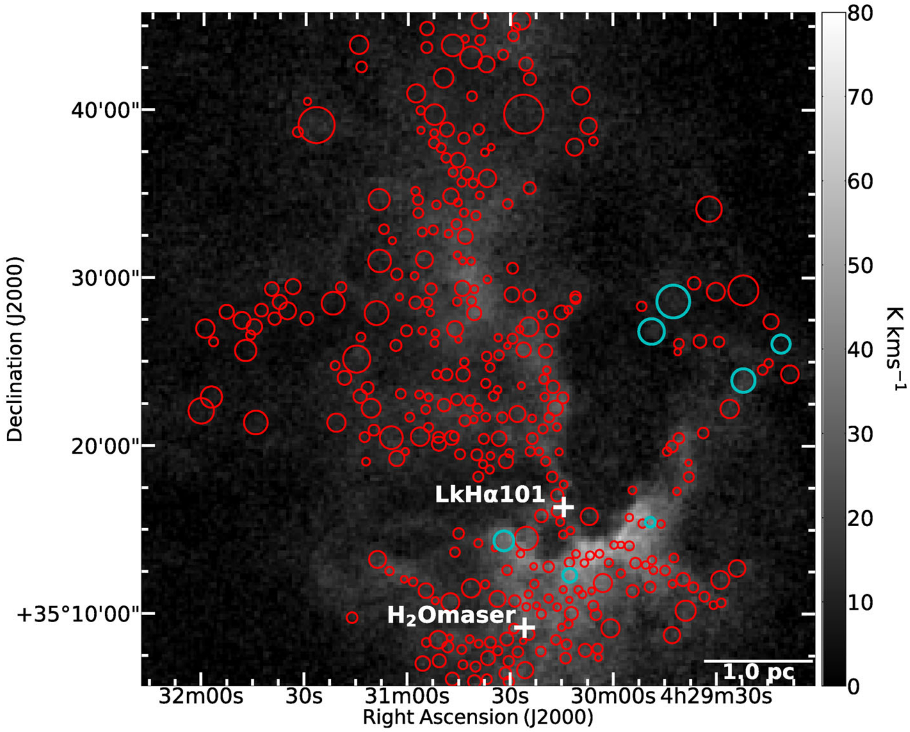

Fig. 8. Integrated intensity map of the $^{13}CO(J = 1–0)$ emission line towards the L 1482 molecular cloud. The circles indicate the locations and diameters of the identified cores.

Table 3. Summary of the physical properties of the core.

	Minimum	Mean	Maximum
R_{core} [pc]	0.029	0.054	0.180
T_{peak} [K]	5.808	12.230	30.578
Background level [K]	6.2	11.3	28.3
ΔV [km s^{-1}]	0.606	1.426	2.674
M_{vir} [$M_\odot$]	3.19	23.55	91.65
$\Sigma N(H_2)$ [$\times 10^{23}$ cm^{-2}]	1.11	6.05	42.69
M_{LTE} [$M_\odot$]	0.76	4.58	35.49
n [$\times 10^4$ cm^3]	0.35	12.96	72.18
M_{vir}/M_{LTE} ($= \alpha_{vir}$)	1.03	6.94	33.23

with a mean value of ∼0.054 pc. The core mass ranges from 0.76 to 35.49 $M_\odot$. We show the summary of the physical parameters of the core in table 3.

Finally, we also derived the total molecular mass of the entire region mapped in ^{13}CO (figure 6) to be ∼7600 $M_\odot$ using the derived T_{ex} and equations (2) and (3).

4 Discussion

4.1 The relation between L 1482 filament and LkHα 101

The measured parallax of the H_2O maser in L 1482 filament 2 is consistent with that of the LkHα 101 cluster measured by VLBA and Gaia DR2. The difference is only 0.01 ± 0.10 mas. The parallax and the proper motion of VLA J043001.15+337724.6 in the LkHα 101 cluster is measured to be $\pi = 1.87 \pm 0.10$ mas and $(\mu_\alpha \cos\delta, \mu_\delta) = (1.86 \pm 0.04, -5.70 \pm 0.05)$ mas yr^{-1} with VLBA radio continuum observations (Dzib et al. 2018). The parallax and the proper motion of LkHα 101 cluster using Gaia DR2 data (Gaia Collaboration 2018) are $\pi = 1.876 \pm 0.051$ mas and $(\mu_\alpha \cos\delta, \mu_\delta) = (2.44 \pm 0.55, -5.27 \pm 0.54)$ mas yr^{-1}, respectively. These are the averages of the parallaxes and the proper motions of 35 sources which are selected from the following three steps:

(i) We selected 178 sources located within 5′ from the center of the LkHα 101 cluster $(\alpha, \delta)_{J2000.0} = (04^h30^m11\overset{s}{.}04, +35°16'44\overset{''}{.}0)$.
(ii) We selected 38 sources whose parallax errors are less than 10%.
(iii) We excluded three foreground sources with parallaxes 3.8, 5.0, and 13.5 mas.

Finally, 35 sources were selected. Figures 9 and 10 show distributions of the parallax and proper motion of the 35 sources. There is a difference of approximately 3 mas yr^{-1} (8 km s^{-1} at 532 pc) in the proper motions between the H_2O maser spot and the LkHα 101 cluster. While the H_2O maser spot is detected at $V_{LSR} = 7.38$ km s^{-1}, the ambient molecular gas in L 1482 filament 2 is detected at $V_{LSR} \simeq -1$ km s^{-1}

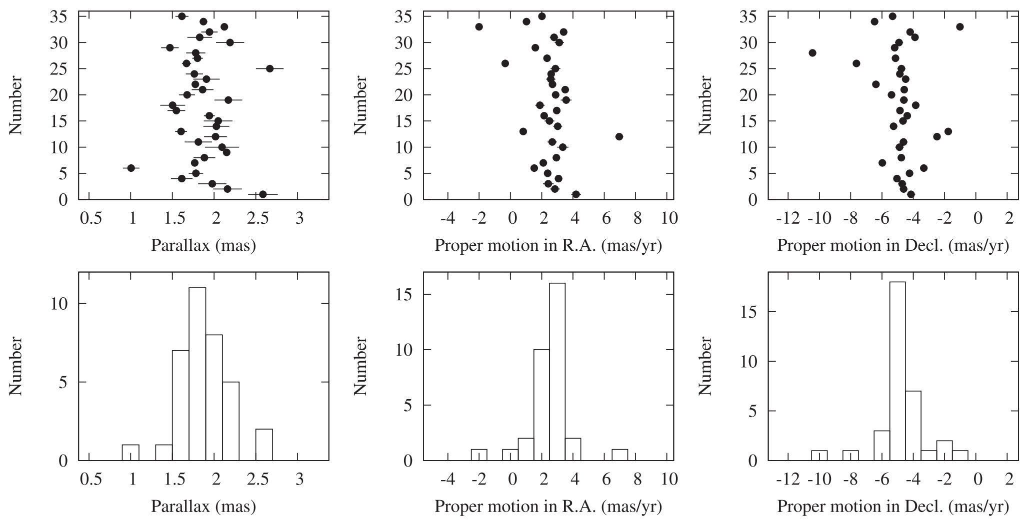

Fig. 9. Distributions of the parallax and proper motion of 35 sources measured by Gaia DR2 (Gaia Collaboration 2018).

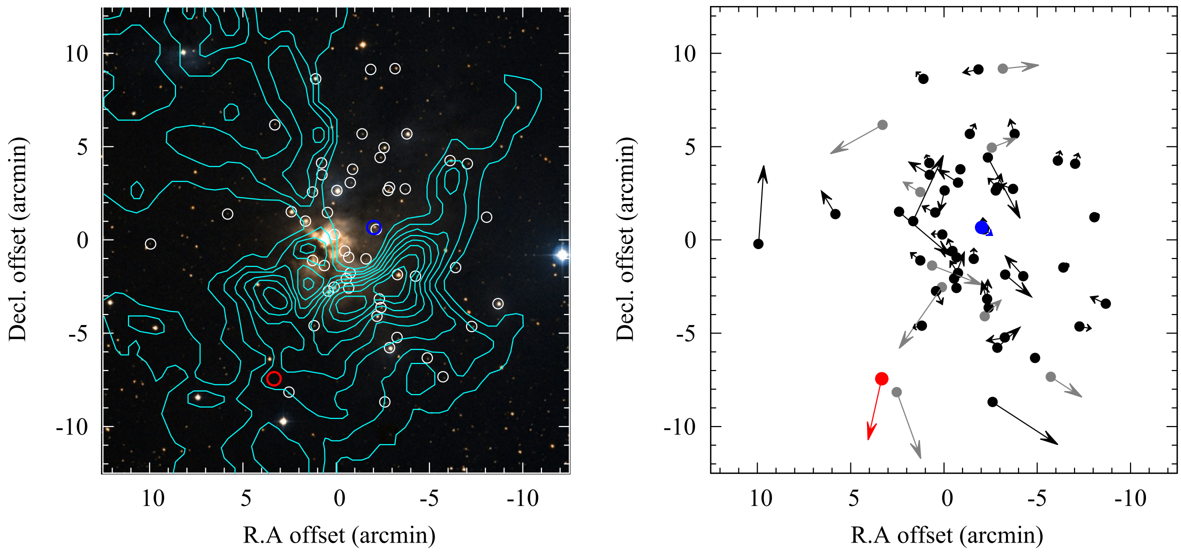

Fig. 10. (Left) Red, blue, and white circles mark the sources observed with VERA (this work), VLBA (Dzib et al. 2018), and Gaia DR2 (Gaia Collaboration 2018), respectively. The background is the Digitized Sky Survey 2 (DSS2) optical image. The cyan contours show the ^{13}CO ($J = 1$–0) integrated intensity (Li et al. 2014). The origin (0, 0) corresponds to $(\alpha, \delta)_{J2000.0} = 04^h30^m11\overset{s}{.}04,\ +35^\circ16'44\overset{''}{.}0$. (Right) Proper motions of the objects represented by the circles. The average of (2.44, −5.27) mas yr^{-1} was removed. One arcminute corresponds to 0.16 pc and 1 mas yr^{-1} corresponds to 2.5 km s^{-1} at the assumed distance 532 pc.

in the ^{13}CO ($J = 1$–0) line (Li et al. 2014). The difference in velocity is approximately 8 km s^{-1}, which may originate from the internal motion of the H_2O maser spot with respect to the associated YSO and/or the peculiar motion of the associated YSO itself. The standard deviations of proper motions of the 35 sources in the LkHα 101 cluster are calculated to be 3.27 mas yr^{-1} and 3.20 mas yr^{-1} in RA and Dec, respectively. This indicates a velocity dispersion of approximately 8.2 km s^{-1}. However, two outlier sources which have large peculiar motions of 36 km s^{-1} and 50 km s^{-1} are included in the 35 sources, and these would lead to the overestimation of the velocity dispersion. We excluded two outlier sources and calculated the standard deviations to be 1.40 mas yr^{-1} and 1.22 mas yr^{-1} in RA and Dec, respectively, indicating the velocity dispersion of approximately 3.3 km s^{-1}. This is close to the average velocity dispersion of 4.5 km s^{-1} calculated for 28 OB-associations (Melnik & Dambis 2020).

4.2 The arc-shaped warm region

It is noted that the warm arc-shaped region surrounds LkHα 101 in the center. The L 1482 molecular filament and the LkHα 101 star cluster are located at the same distance

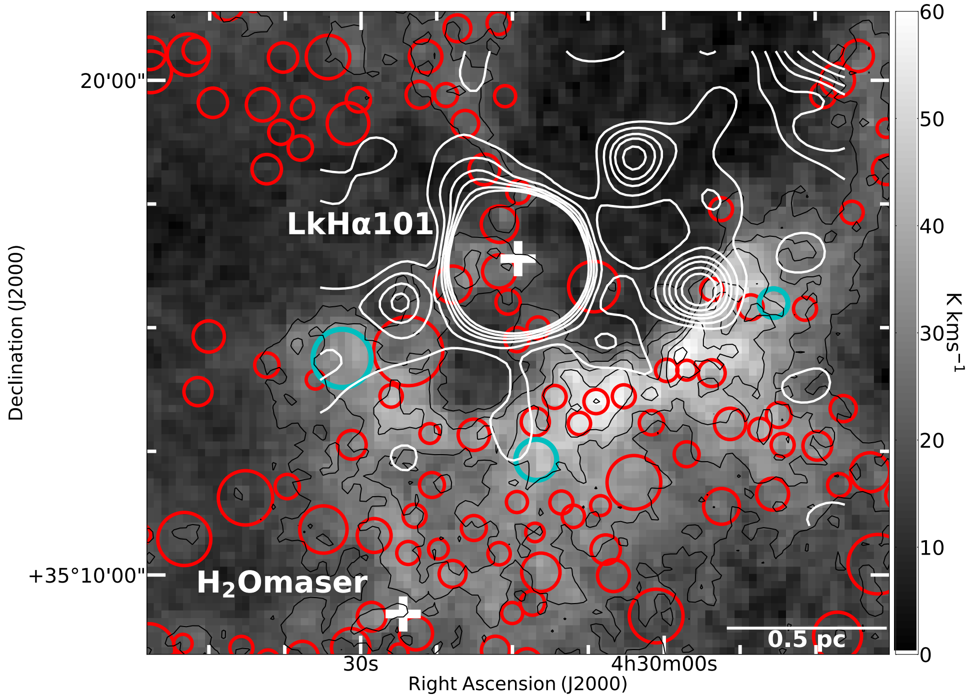

Fig. 11. Integrated intensity map of ^{13}CO ($J = 1$–0) towards the L 1482 molecular cloud overlaid with the VLA 1.4-GHz continuum emission (Condon et al. 1998). The contours start from 0.33 mJy beam^{-1} with an increment of 0.4 mJy beam^{-1}.

within 3 ± 30 pc. This suggests that the warm arc-shaped region is located at the periphery of the H II region ionized by LkHα 101. In order to study the relationship between the warm molecular region and the H II region, we superposed the VLA 1.4 GHz map (taken from Condon et al. 1998) on the ^{13}CO integrated intensity map (see figure 11), which clearly shows that the arc-shaped region is heated by the FUV (6 eV < hν < 13.6 eV) radiation from LkHα 101. The arc-shaped region appears similar to the bright bar in Orion, and can be an ideal region to study photon-dominated region and star formation induced by the interaction with the H II regions created by massive stars.

The thickness of the warm region is about 3′, corresponding to ∼0.46 pc at the distance of 532 pc. Early theoretical model of PDRs (Tielens & Hollenbach 1985a, 1985b; Köster et al. 1994) estimated that the thickness of the region heated by the FUV corresponds to $A_{\rm V} = 10$ mag in visual extinction, being only 0.03 pc assuming hydrogen gas densities $n_{\rm H_2}$ of 10^5 cm^{-3}. As the observed ^{12}CO emission line in PDR regions requires very high hydrogen gas densities, $n_{\rm H_2} = 10^6$–10^7 cm^{-3} (Burton et al. 1990). The emission from the PDR regions facing LkHα 101 may be produced in dense cores embedded in lower-density gas. In the warm region, we often observe a clear dip in the ^{12}CO spectra. As shown in figure 7, the radial velocity of the dip nicely matches with the peak velocity of the optically thinner ^{13}CO emission, indicating that the dip is due to the absorption by a large amount of colder gas lying in the foreground of the warm region. Because the dip is widely seen around the arc-shaped region, the high-temperature gas should be distributed over a considerable extent.

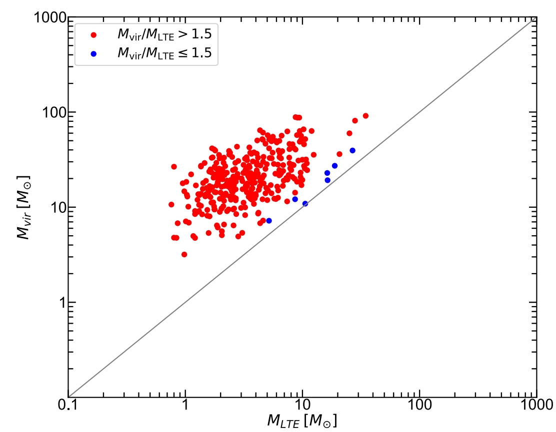

Fig. 12. $M_{\rm vir}$ vs. $M_{\rm LTE}$ relation of the 337 cores found in this study. Blue and red dots indicate cores with $\alpha_{\rm vir} \le 1.5$ and >1.5, respectively.

4.3 Star formation activities in the L 1482 filament

As noted in subsection 3.3, we identified 337 cores using Dendrogram analysis. Figure 12 shows the relation between $M_{\rm vir}$ and $M_{\rm LTE}$ of the 337 cores. As seen in the figure, the virial ratio $\alpha_{\rm vir}(= M_{\rm vir}/M_{\rm LTE})$ is greater than 1. In general,

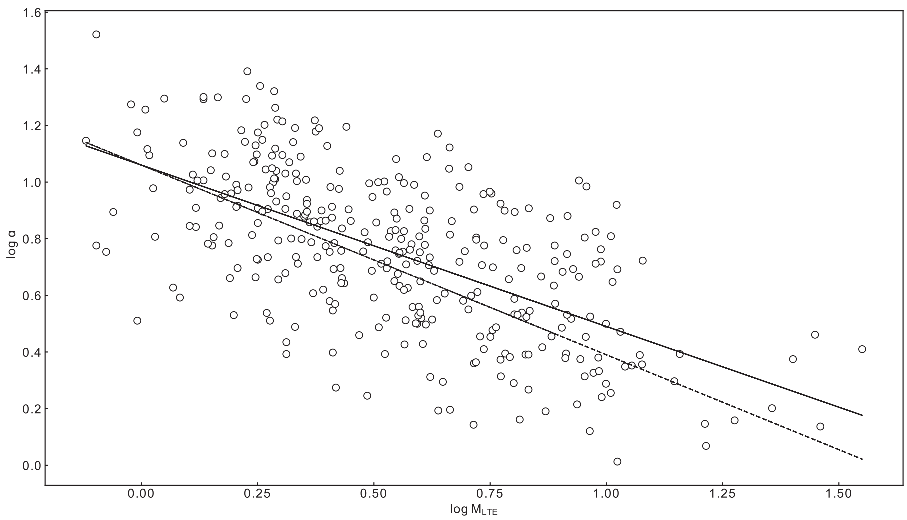

Fig. 13. $M_{\rm LTE}$–α relation of the cores in logarithmic scale. The solid line shows the slope of −0.57 from our data and the dashed line shows the slope of −0.67 of Bertoldi & McKee (1992).

in case there is no external pressure ($P_{\rm ext} = 0$), cores with $\alpha_{\rm vir} < 1$ are gravitationally unstable and are to collapse, while cores with $\alpha_{\rm vir} > 1$ are gravitationally unbound and are to disperse. Shimoikura et al. (2019) who studied massive cores in M 17 suggested that the cores with $\alpha_{\rm vir} > 1$ can also be gravitationally bound, if they are surrounded by high external pressure.

Since the region observed in this study is adjacent to LkHα 101 and a part of the region should be located in the high external pressure of the H II region, some of the cores we detected may be gravitationally bound. Virial ratios of spherical cores with uniform density can reach $\alpha_{\rm vir} = 2$ at most, if they are in the gravitational equilibrium in high external pressure. However, the cores we detected are not perfectly spherical or uniform, and thus we tentatively assume in this paper that cores with $\alpha_{\rm vir} \le 1.5$ are gravitationally bound and that cores with $\alpha_{\rm vir} > 1.5$ are gravitationally unbound. As seen in figure 8, there are seven cores with $\alpha_{\rm vir} \le 1.5$ which are indicated by the blue circles in the figure, and the other cores with $\alpha_{\rm vir} > 1.5$ are indicated by the red circles. Three of the seven cores are located in the photo-dissociated region facing LkHα 101, and the other four cores are found in the northwest of LkHα 101. As is clear from figure 8, the ^{13}CO emission is relatively weak in the northwest region between LkHα 101 and the four cores in the northwest, and the molecular density and therefore the external pressure is likely to be low there. It is noted that the size of the other three cores with $\alpha_{\rm vir} \le 1.5$ adjacent to LkHα 101 is very small compared with the four cores in the northwest, suggesting that the cores close to LkHα 101 are compressed by the high pressure in the H II region. We imagine that these cores may eventually form stars when they become unstable due to increase of the external pressure, e.g., the impact of ionization front of the H II region or strong stellar wind from LkHα 101.

Filaments are noted as the earliest stages of star formation. Theories and models for instabilities and fragmentation of the filament have been extensively studied (e.g., Ostriker 1964; Inutsuka & Miyama 1992). In contrast to the results of those studies, our results show that star formation is unlikely to occur in the massive filamentary structure L 1482 except for the southeast part facing LkHα 101. In the southeast part of the filament adjacent to LkHα 101 and the associated young cluster, the photo-dissociated warm region is formed, and the three cores with $\alpha_{\rm vir} \le 1.5$ are located therein. In this region, there are also protostars associated with H_2O masers. These results suggest that radiation-driven star formation triggered by the expansion of the H II region is proceeding in the southeastern part of the CMC.

Bertoldi and McKee (1992) proposed an $\alpha_{\rm vir} \sim M^{-0.67}$ relation. To test the validity of the exponent of the virial parameter, we made the plot of the core masses against their corresponding $\alpha_{\rm vir}$ (see, figure 13). Our regression fit produced an exponent of −0.57. This is much closer to the −0.54 obtained for the Cepheus cloud (Bertoldi & McKee 1992). This is an indication that L 1482 could be a pressure-confined clump with the possibility of becoming a site of active star formation in the future.

Recently, an ALMA view of the Orion bright bar directly exposed to the Trapezium stars reveals a fragmented ridge of high-density substructures, photo-ablative gas flows, and instabilities at the molecular cloud surface (Goicoechea et al. 2016). Our results show the existence of the high-temperature gas in the warm region where clumpy structures are detected. The possible excitation scenarios of the warm gas are as follows;

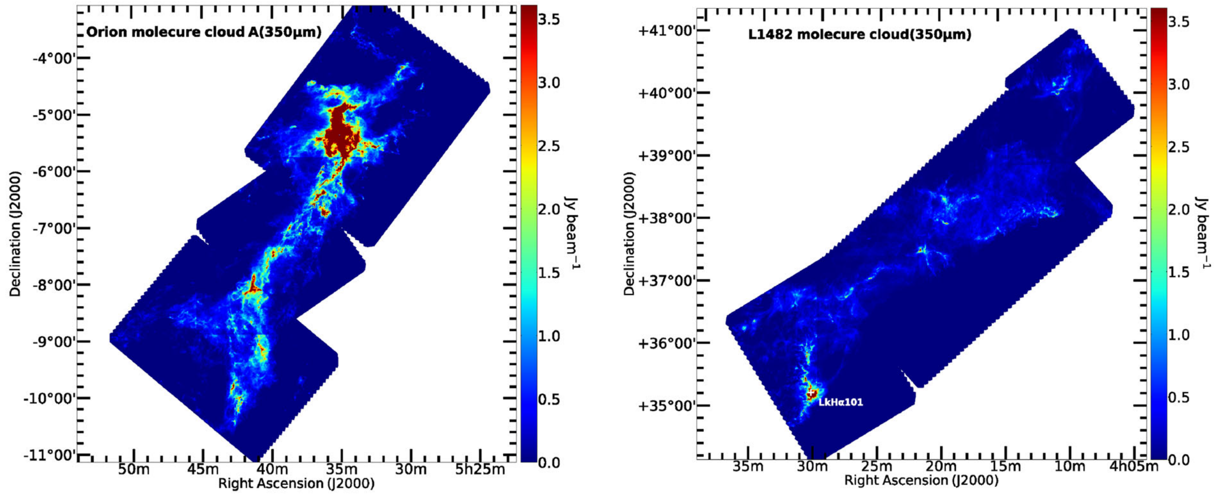

Fig. 14. 350 μm dust continuum emission of the OMC (left) and CMC (right).

(i) the ejection of energetic electrons from dust grains by FUV photons,
(ii) turbulent heating, where the energy stored in local velocity dispersion is thermalized in small-scale shocks (Guesten & Fiebig 1988), and
(iii) photo-ablative high-temperature gas flows as observed in the Orion bar.

At the moment, it remains uncertain which mechanism is the most effective. Also, Goicoechea et al. (2016) suggested that the cloud edge has been compressed by a high-pressure wave that currently moves into the cloud. Our results are consistent with this interpretation. The reasons are as follows;

(1) the warm regions are formed adjacent to B star,
(2) the column density in the warm region is 5–6 times higher than that of surrounding colder regions, and
(3) protostellar cores, an H_2O maser source, and young stars are concentrated in this region.

This suggests that radiation-driven star formation is proceeding in this region.

Finally, we discuss the differences in star formation rates in the CMC and OMC. As noted by Lada et al. (2009), the CMC is very similar in morphology to the Orion A molecular cloud. However, the CMC shows an SFR that is an order of magnitude lower than that of the OMC. Figure 14 shows the 350 μm maps of the CMC (right-hand panel) and OMC (left-hand panel). The map of the CMC is enlarged to the scale of the distance of the OMC. As can be seen in figure 14, there are a number of dense and prominent filaments in the OMC which are known sites of massive star formation, whereas filaments in the CMC are apparently much less dense. According to Krumholz and McKee (2008), a high column density greater than $\sim$1 g cm^{-2} [or $N(H_2) \simeq 10^{23}$ cm^{-2}] is needed for the formation of massive stars. Formation of massive stars should be closely related to the high SFR through the compression of the natal clouds by the powerful stellar wind and the creation of the PDR regions. The critical density ($\sim$1 g cm^{-2}) corresponds to $N(^{13}CO) \simeq 2 \times 10^{17}$ cm^{-2}. Nakamura et al. (2019) recently analyzed the ^{13}CO data observed toward the OMC and found that roughly $\sim$10% of the total mass is confined in dense regions with $N(^{13}CO) > 2 \times 10^{17}$ cm^{-2} (see, their figure 27). The fraction of the high-density regions is much larger in the northern part of the OMC than in the diffuser, and more extended southern part which forms much less massive stars. A similar trend is also found in clouds associated with the M 17 H II region and in rather quiescent infrared dark clouds in the vicinity known as M 17-SWex (Nakamura et al. 2019; Nguyen-Luong et al. 2020). In the case of the CMC, we analyzed the frequency distribution of $N(^{13}CO)$ using our data, and found that there are a very limited number of pixels (only 39 pixels) exceeding the critical value $N(^{13}CO) = 2 \times 10^{17}$ cm^{-2}, and also found that such pixels are located only around the LkHα 101 cluster. This indicates that the mean density of the CMC is not high enough to produce massive stars, which can be one of the major reasons for the low SFR of the CMC compared with the OMC.

5 Conclusions

We have measured the trigonometric parallax of the H_2O maser source associated with the L 1482 molecular filament to be 1.879 $\pm$ 0.096 mas, corresponding to the distance of 532 $\pm$ 28 pc. This parallax is consistent with that of the nearby star cluster, LkHα 101. Our ^{12}CO observations revealed the clumpy arc-shaped, warm structure illuminated by the LkHα 101 cluster. Based on the ^{13}CO observations, we performed core identification, and found 337 cores. Most of the cores are likely to be gravitationally bound and thus they are unlikely to form stars except for some cores located along the arc-shaped structure. The column density in the warm arc-shaped region is 5–6 times higher than that of surrounding colder molecular region, which supports the idea that the radiation-driven star formation triggered by the expansion of the H II region is occurring around the LkHα 101 cluster.

We have also compared the CMC and the OMC, and found the presence of more filamentary structures in the OMC. The OMC has a significantly higher star formation rate compared to the CMC, and the difference may be caused by the fact that nearly all the cores in the L 1482 filament of the CMC are gravitationally stable or unbound and thus they are unable to form stars. We also discussed that the mean density of the CMC is not high enough to produce massive stars, which can be one of the main reasons for the low SFR of the CMC compared with the OMC.

Acknowledgment

We thank to the anonymous referee for the useful comments to our manuscript. Data analysis was [in part] carried out on the Multiwavelength Data Analysis System operated by the Astronomy Data Center (ADC), National Astronomical Observatory of Japan

References

Andrews, S. M., & Wolk, S. J. 2008, in Handbook of Star Forming Regions, Volume I: The Northern, ed. B. Reipurth (San Francisco: ASP), 390
Bertoldi, F., & McKee, C. F. 1992, ApJ, 395, 140
Brittain, S. D., Simon, T., Kulesa, C., & Rettig, T. W. 2004, ApJ, 606, 911
Broekhoven-Fiene, H., et al. 2015, ApJ, 798, 65
Burton, M. G., Hollenbach, D. J., & Tielens, A. G. G. M. 1990, ApJ, 365, 620
Chikada, Y., Kawaguchi, N., Inoue, M., Morimoto, M., Kobayashi, H., & Mattori, S. 1991, in Frontiers of VLBI, ed. H. Hirabayashi et al. (Tokyo: Universal Academy Press), 79
Condon, J. J., Cotton, W. D., Greisen, E. W., Yin, Q. F., Perley, R. A., Taylor, G. B., & Broderick, J. J. 1998, AJ, 115, 1693
Dickman, R. L. 1978, ApJS, 37, 407
Dzib, S. A., Ortiz-León, G. N., Loinard, L., Mioduszewski, A. J., Rodríguez, L. F., Medina, S. N. X., & Torres, R. M. 2018, ApJ, 853, 99
Gaia Collaboration,2018, A&A, 616, A1
Goicoechea, J. R., et al. 2016, Nature, 537, 207
Guesten, R., & Fiebig, D. 1988, A&A, 204, 253
Harvey, P. M., et al. 2013, ApJ, 764, 133
Herbig, G. H., Andrews, S. M., & Dahm, S. E. 2004, AJ, 128, 1233
Honma, M., et al. 2008a, PASJ, 60, 935
Honma, M., Tamura, Y., & Reid, M. J. 2008b, PASJ, 60, 951
Inutsuka, S., & Miyama, S. M. 1992, ApJ, 388, 392
Kawaguchi, N., Sasao, T., & Manabe, S. 2000, in Proc. SPIE, 4015, Radio Telescopes, ed. H. R. Butcher (Bellingham, WA: SPIE), 544
Kong, S., Lada, C. J., Lada, E. A., Román-Zúñiga, C., Bieging, J. H., Lombardi, M., Forbrich, J., & Alves, J. F. 2015, ApJ, 805, 58
Köster, B., Störzer, H., Stutzki, J., & Sternberg, A. 1994, Astron. Ges. Abstr. Ser., 10, 176
Krumholz, M. R., & McKee, C. F. 2008, Nature, 451, 1082
Lada, C. J., Lombardi, M., & Alves, J. F. 2009, ApJ, 703, 52
Li, D. L., Esimbek, J., Zhou, J. J., Lou, Y. Q., Wu, G., Tang, X. D., & He, Y. X. 2014, A&A, 567, A10
Melnik, A. M., & Dambis, A. K. 2020, MNRAS, 493, 2339
Nakamura, F., et al. 2019, PASJ, 71, S10
Nguyen-Luong, Q., et al. 2020, ApJ, 891, 66
Niell, A. E. 1996, J. Geophys. Res., 101, 3227
Omodaka, T. 2009, Assoc. Asia Pacific Phys. Soc. Bull., 19(3), 19
Ostriker, J. 1964, ApJ, 140, 1529
Redman, R. O., Kuiper, T. B. H., Lorre, J. J., & Gunn, J. E. 1986, ApJ, 303, 300
Rosolowsky, E. W., Pineda, J. E., Kauffmann, J., & Goodman, A. A. 2008, ApJ, 679, 1338
Shimoikura, T., Dobashi, K., Hirose, A., et al. 2019, PASJ, 71, S6
Sunada, K., Nakazato, T., Ikeda, N., Hongo, S., Kitamura, Y., & Yang, J. 2007, PASJ, 59, 1185
Sunada, K., Yamaguchi, C., Nakai, N., Sorai, K., Okumura, S. K., & Ukita, N. 2000, in Proc. SPIE, 4015, Radio Telescopes, ed. H. R. Butcher (Bellingham, WA: SPIE), 237
Tielens, A. G. G. M., & Hollenbach, D. 1985a, ApJ, 291, 722
Tielens, A. G. G. M., & Hollenbach, D. 1985b, ApJ, 291, 747
Wilson, T. L., Rohlfs, K., & Hüttemeister, S. 2009, Tools of Radio Astronomy (Berlin: Springer-Verlag)